3D geological characterization of the Hontomín CO_2 storage site, Spain: multidisciplinary approach from seismics, well-logging and regional data.

Authors

Juan Alcalde

Affiliations: Institute of Earth Sciences Jaume Almera ICTJA-CSIC, Barcelona, Spain.

CIUDEN Foundation, Ponferrada, Spain.

Email address: juan.alcalde.martin@gmail.com

Phone no. (+34) 646874631

Ignacio Marzán

Affiliation: Institute of Earth Sciences Jaume Almera ICTJA-CSIC, Barcelona, Spain.

Email address: imarzan@ictja.csic.es

Phone no. (+34) 934095410

Eduard Saura

Affiliation: Institute of Earth Sciences Jaume Almera ICTJA-CSIC, Barcelona, Spain.

Email address: esaura@ictja.csic.es

Phone no. (+34) 934095410

David Martí

Affiliation: Institute of Earth Sciences Jaume Almera ICTJA-CSIC, Barcelona, Spain.

Email address: dmarti@ictja.csic.es

Phone no. (+34) 934095410

Puy Ayarza

Affiliation: University of Salamanca, Salamanca, Spain.

Email address: puy@usal.es

Phone no. (+34) 923294488

Christopher Juhlin

Affiliation: Uppsala University, Uppsala, Sweden.

Email address: christopher.juhlin@geo.uu.se

Phone no. (+46) 018-471 2392

Andrés Pérez-Estaún

Affiliation: Institute of Earth Sciences Jaume Almera ICTJA-CSIC, Barcelona, Spain.

Email address: andres@ictja.csic.es

Phone no. (+34) 934095410

Ramon Carbonell

Affiliation: Institute of Earth Sciences Jaume Almera ICTJA-CSIC, Barcelona, Spain.

Email address: ramon.carbonell@csic.es

Phone no. (+34) 934095410

ABSTRACT

The first Spanish Technological Development plant for CO_2 storage is currently under development in Hontomín (Spain), in a fractured carbonate reservoir. The subsurface 3D geological structures of the Hontomín site were interpreted using well-

log and 3D seismic reflection data. A shallow low velocity zone affects the wave propagation and decreases the coherency of the underlying seismic reflections, deteriorating the quality of the seismic data, and thus preventing a straightforward seismic interpretation. In order to provide a fully constrained model, a geologically supervised interpretation was carried out. In particular, a conceptual geological model was derived from an exhaustive well-logging analysis. This conceptual model was then improved throughout a detailed seismic facies analysis on few seismic sections crossing the seismic wells and in consistency with the regional geology, leading to the interpretation of the entire 3D seismic volume. This procedure allowed characterizing nine main geological levels and four main fault sets. Thus, the stratigraphic sequence of the area and the geometries of the subsurface structures were defined. The resulting depth-converted 3D geological model allowed us to estimate a maximum CO_2 storage capacity of 5.85 Mt. This work provides a 3D geological model of the Hontomín subsurface, which is a challenging case study of CO_2 storage in a complex fractured carbonate reservoir.

1. **Introduction**

Storage of CO_2 in saline aquifers is considered one of the most promising actions for stabilization of atmospheric CO_2 concentrations (Bachu, 2000; IPCC, 2005). The geological storage of CO_2 (GSC) aims to inject this greenhouse gas in an appropriate reservoir site, which requires a suitable reservoir formation (i.e. high porosity and permeability), sealed by a proved competent seal formation (i.e. low porosity and

permeability, lack of conductive faults, etc.), placed at a suitable depth to ensure profitability (e.g. Bachu, 2000; IPCC, 2005; Chadwick et al. 2006; Pérez-Estaún et al., 2009) (Fig. 1). The first Spanish CO_2 storage Technology Development Plant is currently being developed in Hontomín, Spain (Fig. 2), led by the CIUDEN Foundation. The project is carried out in a research and development (R&D) basis, whose objectives focus on the knowledge of strategies for CO_2 injection, testing of monitoring techniques and methodologies and the understanding of the physico-chemical processes associated with CO_2 storage in a deep saline aquifer, through real experiments at the facility.

A number of characteristics determined the suitability of the Hontomín reservoir for GSC (Prado et al. 2008). These included: (1) the existence of a deep saline aquifer, filled with brine (20 g/l of NaCl, Ogaya et al., 2013) and very low oil content; (2) the location of this aquifer within a carbonate reservoir-seal system, allowing mineral trapping-related studies; (3) the acquaintance of a dipping structure, which allows to accelerate the CO_2 migration processes; (4) the relatively small size of the target structure , making it tractable for research purposes; (5) the low seismicity of the area; and (6) the availability of previous information (2D seismic datasets, well-log data) acquired with oil exploration goals.

At the Hontomín site, the target reservoir and seal formations consist of Upper Jurassic marine carbonates, arranged in an asymmetric dome-like structure and located at approximately 1485 m of depth (Ogaya et al., 2013; Alcalde et al., 2013a). The relatively small size of the target structure (approximately 5x3 km^2) facilitates CO_2

monitoring processes. Besides, the existence of structural complexities enable the experimentation related to faults, controlled leakages and remediation techniques.

The Hontomín site presents three main scientific and technical challenges from a GSC point of view. First, it represents one of the first GSC pilot plants implemented in carbonate formations. Carbonate reservoirs possess very interesting attributes for GSC (Bachu et al., 1994): after injection, CO_2 partly dissolves the carbonate rocks (increasing the porosity and permeability, and improving the injectivity), whereas in a long term, the CO_2-saturated brine reacts with the carbonate rocks forcing the precipitation of new minerals and thus ensuring the fixation of the CO_2 in the subsurface (mineral trapping) (Fig. 1).

The second challenge is related to the geological complexity of the study area (Fig.2), which has undergone a very complex and tectono-sedimentary evolution (e.g. García-Mondéjar, 1996; Pujalte et al. 2004; Tavani et al., 2011; Quintà and Tavani 2012; Tavani, 2012; Tavani et al., 2013). This issue is especially important in Hontomín's reservoir and seal formations, which developed fractures under successive deformation stages. In fact, fracturing can have a significant impact on the characteristics of the reservoir system, either increasing or decreasing its secondary porosity and permeability (e.g. Nelson, 2001). Whereas fracturing may enhance secondary porosity and improve the injectivity and capacity of the reservoir, fine fracture filling and, above all, low-permeability fault cores may compartmentalize the reservoir, reducing drastically the reservoir's suitability. Besides, open fractures and highly permeable fault damage zones in the seal formation may significantly reduce its sealing capacity, thus jeopardizing the integrity of the reservoir complex.

Several multidisciplinary experiments have been carried out in the Hontomín site in order to elaborate a 3D Thermo-, Hydro-, Mechanical- and Chemical (THMC) coupled model (e.g. Elío et al., 2012; Alcalde et al., 2013a, 2013b; Canal et al., 2013; Martinez-Landa et al., 2013; Ogaya et al., 2013; Ugalde et al., 2013; Vilamajó et al., 2013). Within them, a 3D seismic reflection dataset was acquired, aiming to obtain a 3D structural and seismic baseline model of the study area (Alcalde et al., 2013b). Carbonate reservoirs may be difficult targets for reflection seismic methods, mainly due to the possible lack of layering during the deposition, diagenetic alterations and other structural complexity-related problems (e.g. Phipps 1989; Rudolph et al., 1989; Kenter et al., 2001; Masaferro et al., 2003; Von Hartmann et al., 2012). These features can frustrate the attempts to characterize the internal structure with seismic reflection methods. In the case of the Hontomín dataset, this issue is stressed by the existence of a near-surface velocity inversion, studied in detail by Alcalde et al. (2013a; 2013b). This velocity inversion generates a “shadow zone” that interrupts the lateral coherency of the reflections in the whole 3D volume.

The complex geology present in Hontomín and the limited quality of the seismic data prevents the application of a conventional straightforward horizon picking in the seismic volume. Therefore, we present an interpretation approach in which seismic facies analysis, well-log correlation and surface geology study are complemented by a conceptual geological model (Fig. 3). Interactive development of the seismic interpretation and the conceptual model leads to the presented geological model. The results obtained by this work enable the understanding of the sedimentary and tectonic history of the Hontomín area, as well as the determination of the feasibility of the reservoir formations for GSC.

2. **Geological setting**

The CO2 storage site of Hontomín is enclosed in the southern section of the Mesozoic Basque-Cantabrian Basin, named “Plataforma Burgalesa” (Serrano and Martínez del Olmo, 1990; Tavani, 2012) (Fig. 2). This domain is located in the northern junction of the Cenozoic Duero and Ebro basins, forming an ESE-dipping monocline bounded by the Sierra de Cantabria Thrust to the North and the Ubierna Fault System to the South (Tavani, 2012).

Three main deformation stages, affected the study area during the Mesozoic and Cenozoic (Tavani, 2012; Tavani et al., 2013). First, a Permian-Triassic extensional stage led to the development of ESE-WNW and E-W trending faults (Ziegler, 1989; García-Mondéjar et al., 1996). The second rifting event, linked to the opening of the North Atlantic and Bay of Biscay (Le Pichon and Sibuet 1971; Montadert et al. 1979; Ziegler 1988; García-Mondéjar et al., 1996) generated the Plataforma Burgalesa along with the Basque-Cantabrian basin. This event inherited ESE-WNW striking faults and generated NNE-SSW striking extensional faults, oriented at an angle of 75-80^{o} with the previous faults (Tavani and Muñoz, 2012; Tavani et al., 2013). During this second rifting event, Upper Triassic Keuper evaporites acted as a major decoupling zone, imposing different deformation styles in the cover sequences and in the Paleozoic basement (Tavani et al., 2011; Alcalde et al., 2013b; Tavani et al., 2013). In particular, this decoupling enabled the development of extensional forced folds in the supra-salt cover, led by coeval evaporite migration and faulting in the sub-salt basement (Tavani et al., 2013). Finally, the latter Pyrenean orogeny originated a compressional environment which caused

reverse, right-lateral and left-lateral reactivations of inherited faults (Tavani et al., 2011; Quintà and Tavani, 2012; Tavani et al., 2013).

From a stratigraphic perspective, the Mesozoic succession in the Hontomín structure (Fig. 4b) starts with the evaporites and clays of the Triassic Keuper Facies, which forms the core of the target dome. The Lower Jurassic is composed of evaporites, dolomites and marls, and lies over the Keuper Facies (Pujalte et al., 2004; Quesada et al., 2005). The upper part of the Lower Jurassic and the Middle Jurassic series is constituted by shallow marine carbonates and hemipelagic ramp sediments which can be divided in four units: Lower Jurassic (1) Carbonate, (2) Marly and (3) Pelletic Lias units and a Middle Jurassic carbonate (4) Dogger unit. The Purbeck Facies (Late Jurassic-Early Cretaceous in age) is formed by clays, sandstone and carbonate rocks, placed uncomformably on top of the Jurassic marine rocks. The Lower Cretaceous succession is completed by siliclastic sediments of the Weald Facies, and the Escucha and Utrillas formations. They are made of fluvial deposits that alternate channel filling sandstones and flood plain shale sediments. The uppermost rocks exposed in the Hontomín area are Upper Cretaceous carbonates and Cenozoic rocks (lacustrine and detritic) lying uncomformably over the Mesozoic successions (Vera, 2004).

The reservoir and seal formations were selected based on the available geophysical and geological data (vintage 2D seismic reflection data, well-logs, borehole core samples, etc.). These formations are Jurassic in age, and form in the Hontomín area a dome-like structure with an overall extent of 5x3 km2. The target CO_2 injection point is a saline aquifer included in the carbonate reservoir-seal system at about 1500 m deep. The target Jurassic formations meets the requirements considered suitable for CO_2

Geological Storage, including physical properties (i.e., porosity, permeability and brine salinity), effective sealing capacity, and depth (Bachu, 2000; Chadwick et al., 2006; Pérez-Estaún et al., 2009). They are formed by a dolostone unit known as “Carniolas” and an oolitic limestone. The estimated porosity of the Carniolas reaches over 12 % (Ogaya et al. 2013) and is slightly lower at the Carbonate Lias level (8.5 % in average). The reservoir levels contain saline water with more than 20 g/l of NaCl. The high porosity of the lower part of the reservoir (i.e., the Carniolas level) is the result of secondary dolomitization and different fracturing events. The minimum thickness of the reservoir units is 100 m. The potential upper seal unit comprises marlstones and black shales from a hemipelagic ramp (Pliensbachian and Toarcian; Vera, 2004).

3. Available data

3D Seismic reflection data

The reflection seismic method constitutes one of the main techniques for the characterization of geological reservoir complexes (e.g., Arts et al., 2001; Martí et al., 2002). A correct seismic characterization is essential to determine the most suitable position for the CO_2 injection (e.g., Juhlin et al., 2007; Alcalde et al., 2013a) and to be used as a baseline in order to track the underground migration of the CO_2 with time-lapse techniques (e.g., Arts et al., 2004; Lumley, 2010; Ivanova et al., 2012; White, 2013).

To accomplish these objectives, a 3D seismic reflection survey was acquired in Hontomín in summer of 2010 (Alcalde et al., 2013a; 2013b) (Fig. 4). The acquisition

parameters included 22 source lines (crosslines), deployed E-W, perpendicular to 22 receiver lines (inlines) deployed N-S, with intervals of 25 m between sources and between receivers; the inline and crossline spacing was 250 m and 275 m, respectively, covering a total extent of 36 km^2. A maximum of 120 channels were active per inline, giving a maximum of 1200 traces per shot gather. This acquisition geometry gave a maximum common depth point (CDP) fold of 36 traces/CDP. Two sources were used in Hontomín: a Vibroseis source (16 s sweep of 8-80 Hz bandwidth), used in the 76% of the source points, and an explosive source (450 g of dynamite distributed in three 1.5 m deep boreholes) used in the remainder 24% source points.

The acquired seismic data was processed down to 1500 ms (Alcalde et al., 2013b). The main applied processing steps include source wavelet matching, static corrections, 3D dip move-out corrections and post stack time migration. A significant effort was made to match the phases of the two used sources. That included the use of trace wide time and phase shifts, which resulted in enhanced reflector continuity and strength. Static corrections resulted to be one of the key processes for obtaining a seismic image suitable for geological interpretation. In the Hontomín dataset, the large topographic changes (up to 200 m) and heterogeneous geology resulted in shifts of over 70 ms per trace on average (Alcalde et al., 2013b).

The existence of an unexpected sharp velocity inversion near the surface, associated to the Upper-Lower Cretaceous contact, severely affected the quality of the data (Alcalde et al., 2013b). This feature reduced the information of the traces corresponding to the position of the shadow zone at offsets larger than 500 m, and decreased the efficacy of

the NMO correction. The final migrated volume, however, provided good quality images of the Hontomín site from 75 to 1350 ms.

Well-log correlation

The well-log correlation was the starting point for the 3D geological modeling of the Hontomín's underground structure. Four oil exploration boreholes lie within the study area (H1, H2, H3 and H4) (Figs. 4a, 5). They were acquired in the late 1960's (H1 and H2), 1991 (H3) and 2007 (H4). The available log data and sampled depths are very uneven, and although they reach the target depths, there is an important lack of data in the upper part of the main logs.

A correlation between the well lithologies and the seismic reflections as accurate as possible is crucial for the interpretation of the seismic data. None of the four wells originally contained a complete sonic log: wells H1, H3 and H4 lack the first 400 m of sonic data, approximately; and well H2, a key well located nearby the expected crest of the Mesozoic structure, lacks it completely. Furthermore, check-shots in these wells were missing or unavailable. This made impossible a preliminary seismic-to-well tie of the data.

At the beginning of 2012 three new wells were drilled for monitoring shallow aquifers (GW1, GW2 and GW3, of 400 m, 400 m and 150 m depth, respectively) (Fig. 4a, 5). These wells provided information of the uppermost layers of the study area, which was especially useful for the incomplete logs. Firstly, a careful interpretation was performed in all the wells, resulting in the identification of 39 well-tops and 12 main levels from the Triassic up to the Cenozoic (Table 1). This interpretation consisted on the

identification of stratigraphic intervals based on all available well logs. Well-log correlation allowed a better and more accurate characterization of the stratigraphic intervals and delimitation of well tops (Fig. 5). Prioritizing modern logs, we then calculated the sonic value averages for the 39 sections delimited by the main well tops. This 1D velocity model was then used to complete the missing sonic log information, allowing a full depth-to-time domain conversion of the wells. With the aim of improving model characterization, we also calculated average values for 4 additional main logs: gamma ray, deep resistivity, bulk density and neutron porosity (shale volume corrected) (Table 1). Unfortunately, the available density and porosity logs lack the first 400 meters, and therefore they could not be completed. The domain conversion of the wells enabled an adequate interpretation of the seismic data. Besides, the data was used to elaborate a lithological and petrophysical prognosis of the injection area, which will be useful for the drilling operations (Fig. 6).

The well-log correlation showed a number of features that conditioned the subsequent seismic interpretation and modeling (Figs. 5 and 6). There were found remarkable thickness variations in the Dogger and Marly Lias sequences between H4 and H2 wells, which are located only 700 meters away. The Dogger thickness variation could be caused by differential erosion, whereas the Marly Lias thickness variation was interpreted as associated to faulting, as discussed below. The H3 well, drilled right on top of a fault, shows a very complex sequence arrangement, cut by 2 main faults and with significant drilling mud losses along the Jurassic sequence.

The shallow, high velocity layer responsible for signal degradation (Alcalde et al., 2013a; and 2013b) is clearly identifiable in the sonic logs of the GW wells. It has been interpreted as the uppermost layer of the Late Cretaceous (KS6, Fig. 6). It is a limestone

layer with velocities up to 4500 m/s (**Table 1**). We believe that this, together with the underlying Utrillas low velocity layer (KU5, Fig. 6), is the main cause of seismic signal degradation (Alcalde et al., 2013a; 2013b). The available logs also allowed us to identify and locate the potential reservoirs and seals in the subsurface of Hontomín, according to their porosity and distribution properties (Table 1).

4. Seismic interpretation

A conventional approach to seismic data interpretation usually includes an appropriate seismic to well tie and the picking of the most interesting reflections through the dataset (e.g. McQuillin et al., 1984; Sheriff and Geldart, 1985; Sopher and Juhlin, 2013). In the Hontomín survey, however, the seismic dataset is characterized by a limited lateral continuity of the reflections, due to the strong influence of the shallow velocity inversion in the wave propagation (Alcalde et al. 2013b). This effect generates disappearances, splits and displacements of the reflections, making complicate or preventing the tracking of a single reflection through different sections. Hence, a different approach to the interpretation was designed (Fig. 3) to take advantage of the available datasets and bias the interpretation in the areas with sparse constrains. This approach begun with the generation of a conceptual 3D model, in which the general structure was outlined from the well-log correlation and regional studies, such as those included in Tavani et al. (2011), Quintà and Tavani (2012) and Tavani et al. (2013), and references therein. Special care was taken in the seismic to well tie. This step was very important due to the relative quality of the seismic dataset. The seismic interpretation process was then performed, using the conceptual model as a reference. The advances in the interpretation were progressively used to readjust the conceptual model and

vice versa, in an iterative way. The final interpretation is a compromise between the seismic and well-log data and regional geology, which supplies in our opinion the best fit solution. However, we are aware that different approaches could provide another interpretation.

Seismic facies analysis

The subsurface is well imaged in the migrated volume from ~75 ms down to ~1350 ms of two-way travel-time (twt) (Figs. 7 and 8). The analysis of the seismic features allowed us to characterize up to 8 different seismic facies, named “A” to “I” from bottom to top (Figs. 7, 8 and 9a, b and c). These facies appear arranged in three domains. The lowermost domain (A and B), is characterized by a section of discontinuous, low amplitude reflections (A), enclosing a brighter set of parallel reflections (B). The A set ranges from 900 ms down to the lower limit of the image. The B set appears unevenly distributed, normally in blocks of less than 50 X 50 CDP and always below 1100 ms twt throughout the whole dataset. The second domain (C and D) shows a characteristic dome-shape structure. It begins with a 200 ms twt thick set of bright reflections (C). It is characterized by an increase of the lateral coherency with respect to the underlying domain, but the boundary between these first two domains is not neat. Set C is roofed by a discontinuous, high amplitude package (D) of approximately 120-200ms. An abrupt vertical offset, along with an increment in the dip of sets C and D is observed at the NE of the H1 well (Fig. 7). The third domain (E-I) contains reflections dipping at a very low angle in the central and northern parts of the study area. A set of bright reflections (E) onlaps the D package in the northern edge of the study area. This E package ranges from 700 ms down to 900 ms twt, and gently dips

towards the N-NE (<3º). This package is overlain by a plane-parallel set of reflections (F) that completely covers the E package and fossilizes the dome structure of the lower domains. The thickness of this package is approximately uniform (~200 ms) at the southern and central part of the cube, and constantly increases towards the north. Above the F set, a low amplitude, occasionally scattered set (G) is observed from 500 ms to the surface. It contains reflection packages with high amplitude and coherency (H) unevenly distributed. Finally, another high amplitude, coherent set (I) can be observed at the SE part of the seismic volume (Fig. 8a). This set is approximately 100 ms thick and displays an overall south dipping attitude on the southern part of the seismic cube.

Age attribution to the described seismic facies was based on well-log data. The first domain includes the lowermost sets, A and B, and was interpreted to contain the basal Triassic and older rocks. The available wells, however, do not reach these depths. Therefore, these data do not provide constraints for either the internal structure within the Triassic sediments, or the depth of the Palaeozoic basement. These Upper Triassic sediments are overlain by the second domain including Jurassic-Lower Cretaceous sediments. It is formed by facies C and D, and the target reservoir and seal formations should be found within this domain. The third domain contains the remainder of the Lower Cretaceous sequence at its bottom (facies E, F, the lower portion of facies G and facies H) and the Late Cretaceous and Cenozoic sediments (Upper part of facies G and facies I).

Seismic Cube Interpretation

To interpret the seismic cube, horizon picking was first performed in profiles "α" (Fig. 7b) and "β" (Fig. 8b), with approximate SW-NE and SE-NW orientations, respectively (Fig. 9d). They are the best constrained profiles in the seismic cube, crossing the oil exploration boreholes: profile α-α' crosses wells H4, H2 and H1, and the profile β-β', wells H3 and H2. Within these two sections, 8 main layers were interpreted (Figs. 7b, 8b and **Table 2**), corresponding to the main units obtained from well-log correlation (Fig. 5). The three lowermost horizons are of special interest from the point of view of the CO_2 injection site since they correspond to the base of the reservoir (top of the Anhydrite Unit, UA), the top of the reservoir (top of the Lias Limestone, LC4) and the top of the seal (top of the Marly Lias, LM5). Five additional overlying layers were also interpreted corresponding to the tops of Dogger, Purbeck, Weald, Escucha and Utrillas formations (JD4, JKP2, KW3, KE2 and KU5, respectively). The seismic interpretation was limited down to the anhydrite unit because of the low signal to noise ratio and the lack of well-log data below this level.

The interpreted α and β profiles were then used as reference for horizon picking following a grid of sections parallel to α and β with an approximate spacing of 250 m, to complete the entire dataset interpretation. This gridding distance, however, was intentionally kept variable, making it denser in the vicinity of conflictive areas (e.g. fault zones, low reflectivity zones, steep horizon changes, etc).

Four types of faults were identified in the seismic cube. An overall scheme of them, with the labelling used during the interpretation can be found in Fig. 9d. The "S-faults" (S-1 to S-3, red dashed lines in Fig. 9d), are located in the southern portion of the study area. Faults S2 and S3 branch from fault S1 and they have a limited along-strike length, compared with the other faults having a similar orientation (i.e. faults N-1 to N-5). This,

coupled with the well-known strike-slip kinematics of fault S1 (that is a splay of the Ubierna right-lateral fault) (Tavani et al., 2011; Quinta and Tavani, 2012), indicates a flower-like assemblage associated with the strike-slip movement of the Ubierna fault. The kinematics of these faults is recorded by wells H3 and H2. These wells show thicker Jurassic-Lower Cretaceous successions (UA-JKP2) on the NW than on the SE fault block, suggesting downward displacement of the northern block during the deposition of these units (Fig. 8). Besides, the JKP2-KW3 interval is thicker in H3 than in H2 and the interval KW3-KU5 shows roughly similar thicknesses on both wells and the Cenozoic succession is about 35 m thick in H3, whereas it is not present in H2. Finally, the KE2-Cenozoic interval is ~110 m higher on the NW wall of these faults, indicating a late uplift of this wall. The “E-faults” (E-1 and E-2, orange dashed lines in Fig. 9d) are located in the eastern portion. Vertical motions along this fault are nicely constraint by wells H1 and H2 on both limbs of this structure. The lower part of the section, from UA to KW3 (Fig. 7), is characterized by a thicker succession on the SW than on the NE wall, indicating a downward displacement of the SW wall during the Jurassic. Besides, the intermediate part (from KW3 to KU5) shows rather homogeneous thicknesses on wells H1 and H2, although the well tops are about ~170 m shallower on the SW than on the NE of the fault, which indicates a post-depositional uplift of the SW fault wall. Finally, the Cenozoic succession is much thicker in Well H1. However, since the top of this succession is eroded in H2, time relationship between fault activity and the sedimentation of this unit cannot be established with the available data (Fig. 7b). The “N-faults” (N-1 to N-5, white dashed lines in Fig. 9d) are small-scale E-W striking and N-dipping normal faults located in the central, northern and western part of the study area. The “X-faults” (X-1 to X-6, yellow dashed lines in Fig. 9d) are small-scale normal

faults placed perpendicularly to the N-faults. Finally, two sets of small scale faults located at the eastern edge of the study area were identified (XE and XS, yellow dashed lines in Fig. 9d). They both lie near the limits of the seismic dataset resolution and far away from well constraints, and therefore the information about their nature and offset cannot be anticipated. However, they show similarities in orientation and development with X-faults, and therefore they have been considered as possible members of this group.

The final interpretation result is an 8-layered, 3D geological model of the entire study volume (Fig. 10 and supplementary material SM1). The depth conversion was performed using the 8-layered velocity model derived from the well-log correlation (Fig. 5). It is noticeable a division of the study area in three blocks delimited by the two major faults, S-1 and E-1 (hereafter “Southern-Fault” and “Eastern-Fault”, respectively): the Eastern, the Central and the Southern block (Fig. 9d). This division is observed in all the interpreted layers (Fig. 10 and supplementary material SM1). Table 2 summarizes the details of heights and thicknesses of all the modelled layers. We will now focus on the four layers that condense the overall underground structure: UA, JD4, KW3 and KU5 (Figs. 11, 12, 13 and 14, respectively). Note that all the depth values indicated in this work are given in meters relative to mean sea level (msl). The UA layer (Fig. 11) ranges from -1085 m to -232 m msl. It defines the top of the Triassic units and the core of the overlying Jurassic structure. It is thoroughly affected by all the described faults (S-, E-, N-, and X-faults), and the result is a staggered shape, especially in the Central-block. In UA, the Central-, Eastern-, and Southern-blocks dip towards NE (~5-18^{o}), NW (~8-25^{o}) and SSW (~5-30^{o}), respectively. The crest of the dome is located near the junction of the South- and East-faults. The JD4 (Fig. 12) depth ranges from -773 m to

+52 m msl. It is the last purely Jurassic layer, and utterly delineates the Jurassic dome-like geometry. It is important to remark the steep vertical offset (up to 140 m) of JD4 across N-1 fault. This offset has a reverse displacement, in clear disagreement with the rest of the N-faults that have a normal displacement. In this layer, the crest of the dome is located near the H2 well, 2 Km to the NE of the culmination of the underlying UA layer. The KW3 layer (Fig. 13) ranges from -384 to 328 m msl. It is only affected by S- and E- faults, and presents an intermediate geometry between the Jurassic and the Cretaceous structure. This geometry is characterized by a reduction in the dips of the Eastern- (~5-20^{o}) and more especially Central-block (~0-8^{o}). On the contrary, the Southern-block increases its dip to 15-30^{o}. The crest of the dome has a small displacement to the N with respect to the underlying JD4, and shows a plateau-like shape. The KU5 (Fig. 14) is theuppermost interpreted layer; it ranges from 191 m to 822 m msl. It still shows a gentle dome structure, which covers the Central-block, and displays clear structural steps associated to the Eastern and Southern faults. The Eastern-block lays about 150 deeper than the Central-block and reduces its dip to 2-10^{o}, while the Southern-block defines a monocline dipping fairly constantly 30-35^{o} to the SW.

5. Discussion

Conceptual modeling and fault timing

The quality of the seismic volume together with the relative geological complexity of the study area prevented a conventional straightforward horizon picking during the interpretation stage. This presents a major practical problem, because the interpretations are not unique. To address this problem, a reference model was set up

by using well-log and seismic data complemented with surface and regional geology as starting points. Certain tectono-sedimentary events were inferred by studying the thickness differences between the 39 interpreted well-tops (Table 1). The criteria used to date these events were based on the distribution of thickness variations for a given interval. When thickness variations were observed along a set of successive formations, these were interpreted as recording an event of differential vertical motions, which given the short distance between wells was assumed to correspond to faulting. Besides, when thickness variation was observed on a single formation, differential erosion was envisaged. These events were checked and correlated with the events outlined in regional works carried out in the study area (e.g., Serrano and Martínez del Olmo, 1990; García-Mondéjar, 1996; Tavani et al., 2011 and 2013; Quintà and Tavani, 2012; Tavani and Muñoz, 2012).

Significant thickness variations were observed within the Liassic (Limestone and Marly) sediments. The α profile (Fig. 7) shows a significant discrepancy in thicknesses between the H4 and H2 wells at the Limestone and Marly Lias levels(Limestone Lias in H2 is twice as thick as in H4). A mud loss, reported in the H4 drilling report in the middle of this level was matched in the seismic volume with the E-W oriented, N-dipping “N-1” fault (Fig. 7b). Several parallel faults with similar characteristics (set N) have been identified, which are fossilized by the top of the Purbeck sediments and separating blocks with varying thicknesses of the underlying Jurassic succession (Fig, 9d and Fig. 15a). These thickness variations suggest that faults of set N were active during the Late Jurassic. Fault N1, however, shows a thicker Weald succession on the southern than on the northern wall, recording that vertical movements on both sides of this fault

extended in time for a longer period than in the remaining faults of set N. The implications of this change in thickness are discussed below.

Fig. 15a shows a portion of profile γ-γ' in which a detail of the geometry and activity of set N is observed. Set N faults are much more developed than Set X faults, which results in a significant structural step, with a drop of ~250 m of the Central block with respect to the Southern Block (Fig. 12). The Marly Lias presents an opposite pattern in terms of thickness: it is 190 m thick in H4 and only 110 m thick in H2. This difference in thicknesses within the relatively short distance between H4 and H2 wells (715 m approximately) suggests the occurrence of an extensional fault that explains the differential sedimentation. This extensional fault was observed as dipping to the S, with an E-W orientation (yellow dashed line in Fig. 7b), and was later identified as a set X fault. This X-fault pattern (small vertical offset, with same orientation and dip) was observed in the entire volume in disconnected faults affecting sediments up to the Marly Lias (Fig. 15b). Thickness variations of the lower part of the Marly Lias succession across set X faults, record their activity during the Late Sinemurian-Pliensbachian. Moreover, there is no seismic evidence of movements of these faults after the sedimentation of the Marly Lias.

The β profile (Fig. 8) also shows a difference in thicknesses between H3 and H2 in the Lias levels. Since H3 well is reported to be located just on top of the Southern fault, we believe that thickness reduction in this well is actually the effect of this fault.

Thickness variations across the Southern and Eastern faults suggest a multistage evolution of these structures. Whereas changes in thickness of the lower part record higher subsidence of the Central-block with respect to the Eastern- and Southern-blocks, seismic, well and surface data indicate that the Central-block is currently

structurally higher than the bounding blocks. We interpret these characteristics as indicating that the Eastern and Southern faults acted as normal faults during the Mesozoic and were later inverted as high angle lateral-reverse faults during the Cenozoic compressional stage. However, the exposure level of the Central-block below the Cenozoic horizon does not permit a more accurate age constraint for the timing of fault inversion. The attitude of these faults in the Jurassic interval, suggests that the Southern fault was part of Set N, whereas the Eastern fault was part of set X.

Geological Evolution of the Hontomín area

The analysis of the seismic facies helped constraining the conceptual model of the evolution of the Hontomín area. The final conceptual model used in the interpretation (Fig. 16-2 and 16-3) includes two main regional deformation stages. The first one occurred during the main Late Jurassic-Early Cretaceous extensional stage (e.g. Ziegler, 1989; Tavani and Muñoz, 2012), and generated E-W trending normal faults. These faults probably triggered or amplified the migration of the Triassic materials towards the dome core and generated associated minor normal faulting affecting the Jurassic-Lower Cretaceous succession, as proposed by Tavani et al. (2013). The second stage of deformation corresponds to the Alpine Orogeny (Late Cretaceous-Cenozoic), which inverted some of the previous faults within a transpressive regime (Tavani and Muñoz, 2012; Tavani et al. 2013).

Surface geometries and fault configuration of the built geological model allow us to propose a geological evolution of the Hontomín dome, which can to some extent be integrated in the regional framework (Fig. 16). This local evolution model focuses on the structures with good age constrain based on exploration wells, and therefore will

only refer to the Post-Triassic evolution of the Hontomín dome. In this model, we propose three main stages affecting the Hontomín structure, according to the identified fault systems (Fig. 16): (1) a local, small scale fracturing stage during Late Lias; (2) a regional fracturing stage during the Late Jurassic-Early Cretaceous extension; and (3) a regional tectonic shortening stage associated to fault inversion, occurring during the Alpine compressional stage.

The Set X faults (Fig. 9d) were described as active during the Liassic period, being confined within the Marly Lias sediments. The overlying Pelletic Limestone unit's thickness is more or less the same in H4 and H2 wells, which suggests that faulting is held below this level. According to previous works, there is an absence of extensional events in the area between the Triassic and the Late Jurassic-Early Cretaceous rifting periods (e.g., Ziegler, 1989; García-Mondéjar, 1996; Quintà and Tavani, 2012; Tavani, 2012; Tavani et al., 2013). A possible origin for these normal faults is that they are associated with normal faults in the basement, originated during the Triassic rifting. These Triassic basement normal faults could produce halokinetic processes associated with differential loading, related to the contrast in thicknesses of the Triassic evaporite sediments on both walls of the basement faults. The salt migration could produce a gentle dome growth and generate normal faults on the flanks (Fig. 16-1). The East-fault was probably originated during this stage, either as an important normal fault or, most probably, as a set of aligned N-S faults, which eventually merged during a later reactivation. Although available non-migrated data below 1.5 s supply some local evidences of faulting at the basement level below the eastern fault, a detailed and accurate geophysical study including the processing of the lower interval of the acquired seismic cube would be necessary for a better comprehension the basement

structure. This would enhance the validation of the halokinetic origin of the Set X faults.

A regional extensional period occurred during the Late Jurassic-Early Cretaceous (Fig. 16-2). During this stage, the E-W north-dipping faults of Set N (Fig. 9d) were formed. Set N is fossilized by the upper Purbeck beds, with the exception of N-1, which as mentioned above was apparently active during the deposition of the Weald materials. Paradoxically, thickness variations of these materials across N-1 suggest a reverse activity of this fault during this period. Possible explanations could be a local inversion related to underlying salt doming, thickness variations associated to strike-slip reactivation, the occurrence of an unidentified, south-dipping normal fault south of N1 or a wrong interpretation of the top Weald horizon. Finally, this fault was also reactivated in a later compressional stage.

During the Late Jurassic-Early Cretaceous extensional stage, the Hontomín dome started a major development by a forced fold mechanism generated by the WNW-ESE Ubierna Fault and the oblique NNE-SSW Hontomín Fault (Tavani et. al., 2013). Another basement normal fault, W-E oriented in this case, forced the folding and the halokinetic growth of the Hontomín dome structure. The Southern Fault, which we attribute to this set, would have originally formed as several minor segments located above a structurally weak zone, which were subsequently merged. The combination of Set N development and salt accumulation below the dome crest is associated with block tilting and differential sedimentation and erosion, which would be the reason for the thickness variation of the Purbeck beds between wells H4 and H2 (Fig. 17).

The third deformation stage took place during the Alpine compression (Fig. 16-3). This stage is characterized by the inversion of previous structures, mostly focused on the

Southern and Eastern faults. At a regional scale, this stage corresponds to the formation of the Ubierna Fault (Fig. 2), a right-lateral fault with reverse component located on the western part of the study zone (Tavani et al., 2011). The location of the Hontomín structure on the SE tip of the Ubierna fault resulted in a significant control by this fault on the final geometry of the Hontomín dome. As a consequence, the Southern fault was mostly inverted as a right lateral strike-slip fault with a small vertical component, whereas the Eastern fault was mostly inverted as a reverse fault with a gentle left-lateral component (Fig. 16-3). The area near the fault N-1 was also reactivated during this process, although some of the resulting deformation was in the form of folding in the uppermost layers, as recorded by the fossilization of this fault by the Purbeck Fm. A slight buckling of the uppermost beds on top of this fault, records mild activity during the successive stages. During Alpine inversion the Triassic materials stacked against the Southern and Eastern faults, increasing the structural relief of the Dome, and the set X faults where passively rotated at the proximities of the main inverted faults. The inversion stage is recorded by the uppermost sediments, deposited during the Late Cretaceous-Cenozoic, defining a step of >450 m across the Southern and N-1 faults, and >250 m across the Eastern fault (Fig. 14).

Theoretical capacity calculation

Several formations have been identified as potential reservoirs and seals throughout the Hontomín site (Table 1). Within them, the Lias Limestone and the Marly Lias were respectively selected as the target reservoir and seal formations, according to Alcalde et al. (2013a). At the reservoir level, the crest of the dome structure is located near the

H2 well. The position of the injection (HI) and monitoring (HA) wells (Fig. 4) was selected aiming to find the maximum gradient direction, which is contained approximately in the H4-H2 direction (Fig. 7; location in Figs. 4 and 9). This geometry will produce a faster migration of the injected CO_2, benefiting the monitoring experiments (Alcalde et al. 2013a).

The detailed 3D model anticipates the existence of an X-set fault between the injection and monitoring boreholes affecting the injection level (Fig. 18). This fault separates two zones suitable for CO_2 injection: one in the W side of the fault ("H4 block" hereafter) and one in the E side of the fault ("H2 block" hereafter) (Fig. 18). The average vertical offset of this fault is 130 m, higher than the total thickness of the reservoir layer and therefore will compartmentalize the reservoir, forming a barrier to the pass of the injected CO_2 between the two blocks. These two potential reservoir blocks are furthermore delimited by the Eastern-fault in the E, the N-1 and N-2 in the S and N respectively, and by another X-like fault in the W (Fig. 18a). Far from considering this compartmentalisation a problem, the presence of this fault adds an interesting challenge in terms of well design and monitoring capacity. By underground deviation of the injection well, the two blocks are accessible from the same position in surface. The H2 block is larger than block H4 (Fig. 18a). However, this does not necessarily mean that the H2 block is more suitable for holding the injection. The amount of CO_2 to be injected is also a fundamental factor in this issue. If only a few tones of CO_2 are to be injected (as is the case of an R&D demonstration plant), it may be of interest to inject CO_2 in a steep zone, which could accelerate the migration of the plume. This could speed up the physical and geochemical processes that take place in the reservoir and seal levels, from the early stages of injection, even with a reduced amount of CO_2

injected in a short period of time. Additionally, injection of CO_2 in block H4 would also supply assessment on the sealing capacity of the fault separating the blocks. The eventual arrival of the CO_2 plume to the monitoring borehole would allow inferring the porosity-permeability parameters of the fault, which can be used in further developments of the storage site.

We have made a broad estimation of the maximum storage capacity of the two blocks, in order to provide a primary evaluation of the two potential scenarios. The H4 block has a total area of $2.366 \cdot 10^6$ m^2. The H2 block's area is larger ($1.076\ 10^7$ m^2), but its dip is slightly lower, which would affect the migration velocity of the CO_2 plume (Alcalde et al., 2013a and 2013b). The total volume of these two blocks ranges from $1.695 \cdot 10^7$ m^3 in the H4 block, to $9.275 \cdot 10^7$ m^3 in the H2 block. We have also calculated pore volume (PV) of the reservoir formation for the two blocks. Assuming an average formation porosity of 8.5 %, obtained from the well-log data, the total PV are $9.94 \cdot 10^5$ m^3 for the H4 block reservoir, and $7.884 \cdot 10^6$ m^3 for the H2 block reservoir.

We have also calculated the maximum theoretical CO_2 storage capacity, assuming a short term storage, and thus considering only the existence of structural and stratigraphic trapping (Bachu et al., 2007; Welkenhuysen et al., 2013), as well as an isotropic distribution of the porosity. This maximum CO_2 storage capacity is calculated as a function of the available storage volume and the density of the CO_2 at the storage conditions:

$$M_{CO_2} = PV \times (1 - S_{wi}) \times \rho_{CO_2} \quad (1)$$

Where M_{CO2} *is* the theoretical storage capacity (kg), PV is the total pore volume (m^3), S_{wi} is the irreducible water (brine in this case) saturation (0-1) and ρ_{CO2} is the density of CO_2 at reservoir conditions (kg/m^3).

The S_{wi} values are usually determined from drainage experiments, which are not yet available in Hontomín. Recent experiments determine that S_{wi} values derived from empirical relationships between porosity, permeability and water saturation (Schlumberger, 1989) are more imprecise and more optimistic compared to experimental data (Torskaya et al., 2007; Bennion and Bachu, 2010). However, since experimental data is also unavailable in Hontomín, we used the empirical relationships given in Schlumberger, 1989 and calculated an approximate S_{wi} value of 0.123, using the porosity values as a reference. We calculated the ρ_{CO2} using the average temperature and pressure conditions at the target depth, obtained from H1-4 wells. By solving the equation of state formulated in Peng and Robinson (1976), the resulting ρ_{CO2} is 745.558 kg/m^3, at average reservoir conditions of 41^o C and 15.3 MPa. With these input values, the calculated maximum theoretical storage capacity is 0.65 Mt of CO_2 for the H4 block reservoir, and 5.2 Mt of CO_2 for the H2 block reservoir. Furthermore, the connectivity of both reservoirs would imply an increase of the overall M_{CO2}, which would be of 5.85 Mt of CO_2.

6. Conclusions

A geologically-supervised interpretation is used to interpret the subsurface structure of the Hontomín dome. This approach is supported by a starting conceptual model that benefits from well-log correlation as first input, and is constrained by a detailed seismic facies analysis and the surface and regional geology This approach allowed detailed delineation of 8 surfaces from Jurassic to Cenozoic and 4 sets of faults, in spite of the limited resolution of a 3D reflection seismic dataset compromised by the existence of a shallow velocity inversion and a complex underground geology.

The geometry of the Hontomín structure is characterised by a central culmination with a continuous domal geometry towards the N and W, but bounded by two major faults in the S and E associated to vertical steps of >450 m and >250 m, respectively. Surface culminations are not vertically stacked and the dip of the dome flanks decreases upsequence, which suggests a protracted although discontinuous growth of the structure. Additionally, two sets of faults have been differentiated, which trend N and E and are associated with the main Southern and Eastern faults.

Detailed analysis of thickness variations across the Hontomín structure and especially across the main faults, allowed differentiating three main stages in the evolution of the dome. The first stage corresponds to the development of N-trending faults and is recorded by differential deposition of the lowermost Jurassic (Marly Lias) units. These faults could have been originated by salt movements produced by differential loading related to W-E oriented basement faults, originated in the Triassic rifting event. These movements could have produced a forced folding and the halokinetic growth of the Hontomín dome structure. The second stage corresponds to the development of the East-trending faults and is recorded by the deposition of the Purbeck deposits. This stage occurred within a regional extensional regime related to the opening of the Bay of Biscay, and is related to the migration of the Triassic materials towards the dome core, which enhanced its growth. The third and final stage occurred during the Pyrenean orogeny and was mainly characterised by the reactivation and inversion of the South and East faults and the further development of the domal structure, as recorded by the syn-kinematic Cenozoic sediments.

The 3D model of the Hontomín structure provides a challenging scenario for the testing of CO_2 storage. With a maximum theoretical CO_2 storage capacity of 5.85 Mt and the occurrence of early faults compartmentalising the reservoir, monitoring of the evolution of an injected CO_2 plume is expected to supply a high quality model of the behaviour of CO_2 in fractured carbonate reservoirs to be used in the development of future CO_2 storage sites.

ACKNOWLEDGEMENTS

The authors sincerely thank the Guest Editor Irina Artemieva and the two anonymous reviewers for their useful comments. Funding for this Project has been partially provided by the Spanish Ministry of Industry, Tourism and Trade, through the CIUDEN-CSIC-Inst. Jaume Almera agreement (Characterization, Development and Validation of Seismic Techniques applied to CO_2 Geological Storage Sites) and by the European Union through the Technology Demonstration Plant of Compostilla OXYCFB300 Project (European Energy Programme for 534 Recovery). Additional support has been provided by Spanish Ministry of Education Science (CSD2006-00041), Generalitat de Catalunya (2009SGR006) and CSIC JAE-Doc postdoctoral research contract (E.S.). The sole responsibility of this publication lies with the authors. The European Union is not responsible for any use that may be made of the information contained herein. Juan Alcalde is being currently supported by the Fundación Ciudad de la Energía (CIUDEN) Research training program. The authors would like to sincerely thank Javier Elío for his kind help with the capacity estimation calculations, Institut Geològic de Catalunya for their useful work with the GWs, GEMODELS/UB and to all the people involved directly or indirectly in the elaboration of this work.

References

Alcalde et al., 2013a: Alcalde, J., Martí, D., Calahorrano, A., Marzán, I., Ayarza, P., Carbonell, R., Juhlin, C. and Pérez-Estaún, A., 2013a. Active seismic characterization experiments of the Hontomín research facility for geological storage of CO_2, Spain. International Journal of Greenhouse Gas Control. Volume 19, pp. 785–795.DOI: http://dx.doi.org/ 10.1016/j.ijggc.2013.01.039

Alcalde et al., 2013b: Alcalde, J., Martí, D., Juhlin, C., Malehmir, A., Sopher, D., Saura, E., Marzán, I., Ayarza, P., Calahorrano, A., Pérez-Estaún, A., and Carbonell, R., 2013b. 3-D reflection seismic imaging of the Hontomín structure in the Basque–Cantabrian Basin (Spain), Solid Earth, 4, 481-496.DOI:10.5194/se-4-481-2013.

Arts et al., 2001: Arts, R., Brevik, I., Eiken, O., Sollie, R., Causse, E., Van Der Meer, B., 2001. Geophysical methods for monitoring marine aquifer CO_2 storage Sleipner experiences. Proceedings of the 5th International Conference on Greenhouse Gas Control Technologies, CSIRO Publishing.

Arts et al., 2004: Arts, R., O. Eiken, A. Chadwick, P. Zweigel, L. van der Meer, and B. Zinszner 2004. Monitoring of CO_2 injected at Sleipner using time-lapse seismic data, *Energy*, *29*(9-10), 1383-1392.

Bachu et al., 1994: Bachu, S., Gunter, W. D., and Perkins, E.H., 1994. Aquifer disposal of CO_2: hydrodynamic and mineral trapping, Energy Conversion and Management, v. 35, p. 269-279.

Bachu, 2000: Bachu, S., 2000. Sequestration of CO_2 in geological media: criteria and approach for site selection in response to climate change. Energy Conversion and

Management, Volume 41, Issue 9, 1 June 2000, Pages 953-970, DOI: 10.1016/S0196-8904(99)00149-1.

Bachu et al., 2007: Bachu, S., Bonijoli, D., Bradshaw, J., Burruss, R., Holloway, S., Christensen, N.P., Mathiassen, O.M., 2007. CO_2 storage capacity estimation: methodology and gaps. International Journal on Greenhouse Gas Control, 1, 430–443.

Bennion and Bachu, 2010: Bennion, D.B., Bachu, S., 2010. Drainage and imbibition CO_2/brine relative permeability curves at reservoir conditions for carbonate formations. In: SPE Paper 134028, SPE Annual Conference and Exhibition, Florence, Italy

Canal et al., 2013: Canal, J., Delgado, J., Falcón, I., Yang, Q., Juncosa, R., and Barrientos, V., 2013. Injection of CO_2-saturated water through a siliceous sandstone plug from the Hontomín Test Site (Spain): experiments and modeling. Environ. Sci. Technol. 47, 159-167.

Chadwick et al., 2006: Chadwick, A., Arts, R., Bernstone, C., May, F., Thibeau, S., Zweigel, P., 2006. Best practice for the storage of CO_2in saline aquifers. Keyworth, Nottingham: British Geological Survey Occasional Publication, No. 14.ISBN: 978-0-85272-610-5.

Förster et al., 2006: Förster, A., Norden, B., Zinck-Jørgensen, K., Frykman, P., Kulenkampss, J., Spangerberg, E., Erzinger, J., Zimmer, M., Kopp, J., Borm, G., Julin, C., Cosma, C., and Hurter, S. 2006. Baseline characterization of the CO2SINK geological storage site at Ketzin, Germany. Environmental Geosciences, *13*(3), 145-161.

García-Mondéjar, 1996: García-Mondéjar, J., 1996, Plate reconstruction of the Bay

of Biscay. Geology, 24, 635–638.

Ivanova et al., 2012: Ivanova, A., Kashubin, A., Juhojuntti, N., Kummerow, J., Henninges, J., Juhlin, C., Lüth, S. and Ivandic, M., 2012. Monitoring and volumetric estimation of injected CO_2 using 4D seismic, petrophysical data, core measurements and well logging: a case study at Ketzin, Germany. Geophysical Prospecting, 60, 957-973. doi: 10.1111/j.1365-2478.2012.01045.x

Juhlin et al., 2007: Juhlin, C., Giese, R., Zinck-Jørgensen, K., Cosma, C., Kazemeini, H., Juhojuntti, N., Lüth, S., Norden, B., Förster, A., 2007. 3D baseline seismics at Ketzin, Germany: The CO2SINK project. Energy Procedia, 1, 2029-2035.

Kenter et al., 2001: Kenter, J.A.M., Bracco Gartner, G.L., Schlager, W., 2001, Seismic models of a mixed carbonate-siliciclastic shelf margin: Permian upper San Andres Formation, Last Chance Canyon, New Mexico. Geophysics, 66 (6), pp. 1744-1748.

Le Pichon and Sibuet: Le Pichon, X., and Sibuet, J. C., 1971. Western extension of boundary between European and Iberian plates during the Pyrenean orogeny. Earth Planetary Scientific Letters, 12, 83-88.

Lumley, 2010: Lumley, D., (2010), 4D seismic monitoring of CO_2 sequestration, *Leading Edge (Tulsa, OK)*, *29*(2), 150-155.

Masaferro et al., 2003: Masaferro, J., Bourne, R., and Jauffred, J., 2003. 3D visualization of carbonate reservoirs. The Leading Edge, 22 (1), 18–25. doi: 10.1190/1.1542751

Martinez-Landa, L. et al,. 2013: Martinez-Landa, L., Rötting, T., Carrera, J., Russian, A., Dentz, M., and Cubillo, B., 2013. Use of hydraulic tests to identify the residual

CO_2saturation at a geological storage site. International Journal of Greenhouse Gas Control (2013), http://dx.doi.org/10.1016/j.ijggc.2013.01.043

Mc Quillin et al., 1984: McQuillin, R., Bacon, M., Barclay, W., 1984. An introduction to seismic interpretation: reflection seismics in petroleum exploration. Second edition., 287 p.

Montadert et al., 1979: Montadert, L., de Charpal, O., Roberts, D., Guennoc, P., Sibuet, J.C., 1979. Northeast Atlantic passive continental margins: rifting and subsidence processes. In: Talwani, M., Hay, W., Ryan, W.B.F. (Eds.), Deep Drilling Results in the Atlantic Ocean: Continental Margins and Paleoenvironment. Maurice Ewing Ser., vol. 3. AGU, Washington, DC, pp. 154–186, http://dx.doi.org/10.1029/ME003p0154.

Nelson, 2001: Nelson, R. A., 2001. Geologic Analysis of Naturally Fractured Reservoirs (Second edition), Gulf Professional Publishing, Woburn, 2001, ISBN 9780884153177

Nisi et al., 2013: Nisi, B., Vaselli, O., Tassi, F., de Elio, J., Huertas, A.D., Mazadiego, L.F., Ortega, M.F., 2013. Hydrogeochemistry of surface and spring waters in the surroundings of the CO_2 injection site at Hontomín-Huermeces (Burgos, Spain). International Journal of Greenhouse Gas Control, 14, pp. 151-168.

IPCC 2005: IPCC – Intergovernmental Panel on Climate Change, 2005. IPCC Special Report on Carbon Dioxide Capture and Storage. Cambridge University Press, Cambridge, UK, pp. 195–276 (Chapter 5).

Ogaya et al., 2013: Ogaya, X., Ledo, J., Queralt, P., Marcuello, A. and Quintà, A., (2013), First geoelectrical image of the subsurface of the Hontomín site (Spain) for

CO_2geological storage: A magnetotelluric 2D characterization, *International Journal of Greenhouse Gas Control,* 13, 168-179.

Peng and Robinson, 1976: Peng, D.-Y., and Robinson, D. B., 1976, A New Two-Constant Equation of State: Ind. Eng. Chem., Fundam., 15, 59-64.

Pérez-Estaún et al., 2009: Pérez-Estaún, A., Gómez, M. and Carrera, J., 2009. El almacenamiento geológico de CO_2, una de las soluciones al efecto invernadero. Enseñanza de las Ciencias de la Tierra, (17.2), 179-189.

Phipps, 1989: Phipps, G.G., 1989. Exploring for dolomitized Slave Point carbonates in northeastern British Columbia. Geophysics, 54 (7), 806-814.

Pujalte et al., 2004: Pujalte, V., Robles, S., García-Ramos, J. C. and Hernández, J. M., (2004), El Malm-Barremiense no marinos de la Cordillera Cantábrica. Geología de España(J.A. Vera, Ed), SGE-IGME, Madrid, pp 288-291.

Quesada et al., 2005: Quesada, S., Robles, S., Rosales, I., 2005. Depositional architecture and transgressive–regressive cycles within Liassic backstepping carbonate ramps in the Basque-Cantabrian basin, northern Spain. Journal of the Geological Society 162 (3), 531–538.

Quintà and Tavani, 2012: Quintà, A., and Tavani, S, (2012). The foreland deformation in the south-western Basque-Cantabrian Belt (Spain).Tectonophysics, 576-577 (2012) 4-19.

Quintà et al., 2012: Quintá, A., Tavani, S. and Roca, E., 2012. Fracture pattern analysis as a tool for constraining the interaction between regional and diapir-related stress

fields: Poza de la Sal Diapir (Basque Pyrenees, Spain). Geological Society, London, Special Publications. V 363,pp. 521-532. DOI: 10.1144/SP363.25

Rudolph et al., 1989: Rudolph, K.W., Schlager, W., Biddle, K.T., 1989. Seismic models of a carbonate foreslope-to-basin transition, Picco di Vallandro, Dolomite Alps, northern Italy, *Geology*, 17 (5), pp. 453-456. ISSN: 00917613

Serrano and Martinez del Olmo, 1990: Serrano, A., and Martinez del Olmo, W. 1990. Tectonicasalina en el Dominio Cantabro–Navarro: evolucion,edad y origen de las estructuras salinas. In: Orti, F.&Salvany, J. M. (eds) Formaciones evaporiticas dela Cuenca del Ebro y cadenas perifericas, y de lazona de Levante. Nuevas Aportaciones y GuiadeSuperficie. Empresa Nacional De Residuos RadiactivosS.A, ENRESA-GPPG, Barcelona, 39–53.

Sheriff and Geldart, 1985: Sheriff, R.E. and Geldart, L.P., 1985. Exploration seismology.Data-processing and interpretation, vol. 2. Cambridge University Press, New York.

Sopher and Juhlin, 2013: Sopher, D., and Juhlin, C., 2013. Processing and Interpretation of vintage 2D marine seismic data from the outer Hanö Bay Area, Baltic Sea.Journal of Applied Geophysics.doi: 10.1016/j.jappgeo.2013.04.011

Schlumberger, 1989: Schlumberger. 1989. Log interpretation Principles/Applications.Schlumberger Wireline & Testing, Sugar Land, Texas, USA.

Tavani et al., 2011: Tavani, S., Quintà, A., and Granado, P., 2011. Cenozoic right-lateral wrench tectonics in the Western Pyrenees (Spain): The Ubierna Fault System. Tectonophysics, 509, 238-253.

Tavani, 2012: Tavani, S., 2012. Plate kinematics in the Cantabrian domain of the Pyrenean orogen. Solid Earth, 3, 265-292.

Tavani and Muñoz, 2012: Tavani, S., and Muñoz, J. A., 2012. Mesozoic rifting in the Basque-Cantabrian Basin (Spain): Inherited faults, transversal structures and stress perturbation. Terra Nova, 24, 70-76.

Tavani et al., 2013: Tavani, S., Carola, C., Granado, P., Quintà, A., Muñoz, J. A., 2011. Transpressive inversion of a Mesozoic extensional forced fold system with an intermediate décollement level in the Basque-Cantabrian Basin (Spain). Tectonics, 32. doi:10.1002/tect.20019.

Torskaya et al., 2007: Torskaya, T., Jin, G., Torres-Verdin, C., 2007. Pore-level analysis of the relationship between porosity, irreducible water saturation, and permeability of clastic rocks. Proceedings - SPE Annual Technical Conference and Exhibition, 2, pp. 1331-1339.

Ugalde et al., 2013: Ugalde, A., Villaseñor, A., Gaite, B., Casquero, S., Martí, D., Calahorrano, A., Marzán, I., Carbonell, R., Estaún, A.P., 2013. Passive seismic monitoring of an experimental CO_2 geological storage site in Hontomín (Northern Spain).SeismologicalResearchLetters, 84 (1), pp. 75-84.

Vera, 2004: Vera, J. A., 2004. Geología de España. SGE-IGME, Madrid, pp. 890.

Vilamajó et al., 2013: Vilamajó, E., Queralt, P., Ledo, J., Marcuello, A., 2013. Feasibility of Monitoring the Hontomín (Burgos, Spain) CO_2 Storage Site Using a Deep EM Source. Surveys in Geophysics, 34 (4), pp. 441-461.

Von Hartmann et al., 2012: Von Hartmann, H., Buness, H., Krawczyk, C.M., Schulz, R., 2012. 3-D seismic analysis of a carbonate platform in the Molasse Basin - reef distribution and internal separation with seismic attributes.Tectonophysics, 572-573, pp. 16-25. DOI: 10.1016/j.tecto.2012.06.033

White 2013: White, D., 2013. Seismic characterization and time-lapse imaging during seven years of CO_2 flood in the Weyburn field, Saskatchewan, Canada. International Journal of Greenhouse Gas Control. -*In press*-

Welkenhuysen et al., 2013: Welkenhuysen, K., Ramírez, A., Swennen, R., Piessens, K., 2013. Strategy for ranking potential CO_2 storage reservoirs: A case study for Belgium, International Journal of Greenhouse Gas Control, Volume 17, pp 431-449, http://dx.doi.org/10.1016/j.ijggc.2013.05.025.

Ziegler 1989: Ziegler, P. A., 1989. Evolution of the North Atlantic: An Overview. AAPG Memoir, 46, in A. J. Tankard, H. R. Balkwill Editors, Extensional Tectonics and Stratigraphy of the North Atlantic Margins, 111-129.

Table captions

Table 1: Main characteristics of the 39 interpreted well-tops. The five last columns are mean values for the main logs: gamma ray (GR), sonic (DT), bulk density (RHOB), neutron porosity (shale volume corrected; Nϕ-Vsh) and deep resistivity (Res_D).

Table 2: Main position values for the 8 layers interpreted. *: Relative to sea level, in meters.

Figure captions

Fig. 1: Scheme of favorable and unfavorable scenarios for geological storage of CO_2.

Fig. 2: (a) Location of the study area within the Iberian Peninsula, and geological map of the Basque-Cantabrian Basin and Asturian Massif area with labels of the main features (modified from Tavani et al., 2013); (b) geological map of the southern portion of the Basque-Cantabrian Basin, with detail of the Plataforma Burgalesa and the Hontomín location (modified fromTavani et al. 2011).

Fig. 3: Strategy for the generation of the 3D geological model. The well-log data was used as starting point for the conceptual modelling, which was then combined with the 3D seismic data and complemented with surface and regional geology.

Fig.4: (a) Detail of the main geological features of the study area, with the position of the 3D seismic survey (black square), the location of the wells used in the modelling and the injection (Hi) and monitoring (Ha) wells; (b) Synthetic stratigraphic log based on available seismic and well data.

Fig.5: 3D stratigraphic correlation of exploration wells H1, H2, H3 and H4, based on the sonic, GR, resistivity and bulk density logs. The well interpretation is referenced to the top of the Purbeck Fm.

Fig. 6: Lythological and petrophisical prognosis of the injection position (Hi). It includes well-log interpolations for GR, sonic, bulk density, neutron porosity (shale volume-corrected), resistivity and lythology. Location of Hi in Fig. 3a; details of the variables and values in Table 1.

Fig. 7: First 1300 ms of the migrated section α-α' (location marked inFig. 3a) with (a) an analysis of the main seismic facies observed, and (b) the final interpretation of the main horizons (continuous lines) and faults (dashed lines). The well-tops from wells H4, H2 and H1 are included. The white crosses mark the well positions intersected by faults (from well-logs).

Fig. 8: First 1300 ms of the migrated section β-β' (location marked in Fig. 4a) with (a) an analysis of the main seismic facies observed, and (b) the final interpretation of the main horizons (continuous lines) and faults (dashed lines). The well-tops from wells H3 and H2 are included. The white crosses mark the well positions intersected by faults (from well-logs).

Fig. 9: Time slices with the main horizons (continuous lines) and fault distribution (dashed lines) interpreted at (a) 650 ms; (b) 800 ms; and (c) 1000 ms twt; and (d) general distribution and labelling of the main faults interpreted in the study area. The position of profiles α-α', β-β', γ-γ', δ-δ' and of the wells is shown.

Fig. 10: 3D visualization of the resulting 8-layered geological model (a and b) and detail of the target dome structure (Jurassic) (c and d).

Fig. 11: Depth map and 3D perspective view of the interpreted UA layer (top of the Anhydrite Unit). The dashed lines in the map represent the faults affecting this layer (description and labelling in Fig. 9d).

Fig. 12: Depth map and 3D perspective view of the interpreted JD4 layer (top of the Dogger Unit). The dashed lines in the map represent the faults affecting this layer (description and labelling in Fig. 9d).

Fig. 13: Depth map and 3D perspective view of the interpreted KW3 layer (top of the Weald Unit). The dashed lines in the map represent the faults affecting this layer (description and labelling in Fig. 9d).

Fig. 14: Depth map and 3D perspective view of the interpreted KU5 layer (top of the Utrillas Unit). The dashed lines in the map represent the faults affecting this layer (description and labelling in Fig. 9d).

Fig. 15: Portion of profiles a) δ-δ’ and b) γ-γ’ with the final interpretation of the main horizons (continuous lines) and the detail of the geometry of set X- (yellow dashed lines in a) and N-faults (white dashed lines in b).

Fig. 16: The sequence of the three main geological events for the zone. Pink color represents the Keuper detachment level. 1) E-W Triassic evaporites migration during deposition of Marly Lias produces a slight accommodation folding of the Trias-Lias cover and poor development if normal faults, shaping a N-S oriented anticline. 2) N-S extension during deposition of Purbeck produces faulting on the basement and covers and triggers N-S salt migration and shapes a dome-like structure. 3) NW-SE Cenozoic compression breaks the structure reactivating and inverting the mains east (E1) and south (S1) faults produces a wedge-thrusting of the NW block. The green dashed line represents a Cretaceous layer onlapping the dome-like structure.

Fig. 17: Scheme of the tilting of the Dogger blocks forced by the normal faulting and the dome growth, and resultant differential sedimentation in the covering Purbeck layer (also observed in the well interpretations).

74 Fig. 18: a) Position of the two potential CO_2 reservoirs, the H4-block and H2-block,
75 limited by N-1, N-2, E-1, and two X-2 faults at S, N, E and W, respectively. b) Zoom of
76 the potential reservoirs with the two trapping mechanisms available: fault trapping for
77 the H4-block and anticlinal trapping for the H2-block.

78

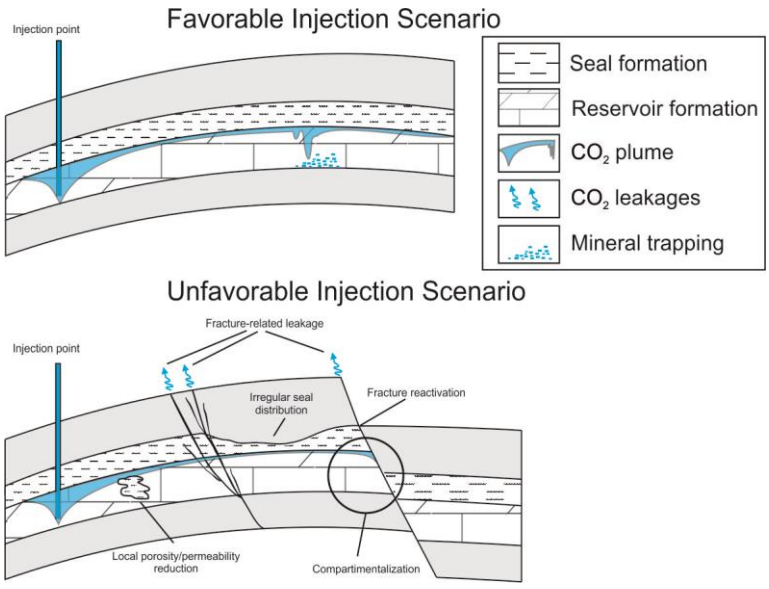
Favorable Injection Scenario
Injection point
Seal formation
Reservoir formation
CO_2 plume
CO_2 leakages
Mineral trapping
Unfavorable Injection Scenario
Fracture-related leakage
Injection point
Irregular seal distribution
Fracture reactivation
Local porosity/permeability reduction
Compartimentalization

79
80

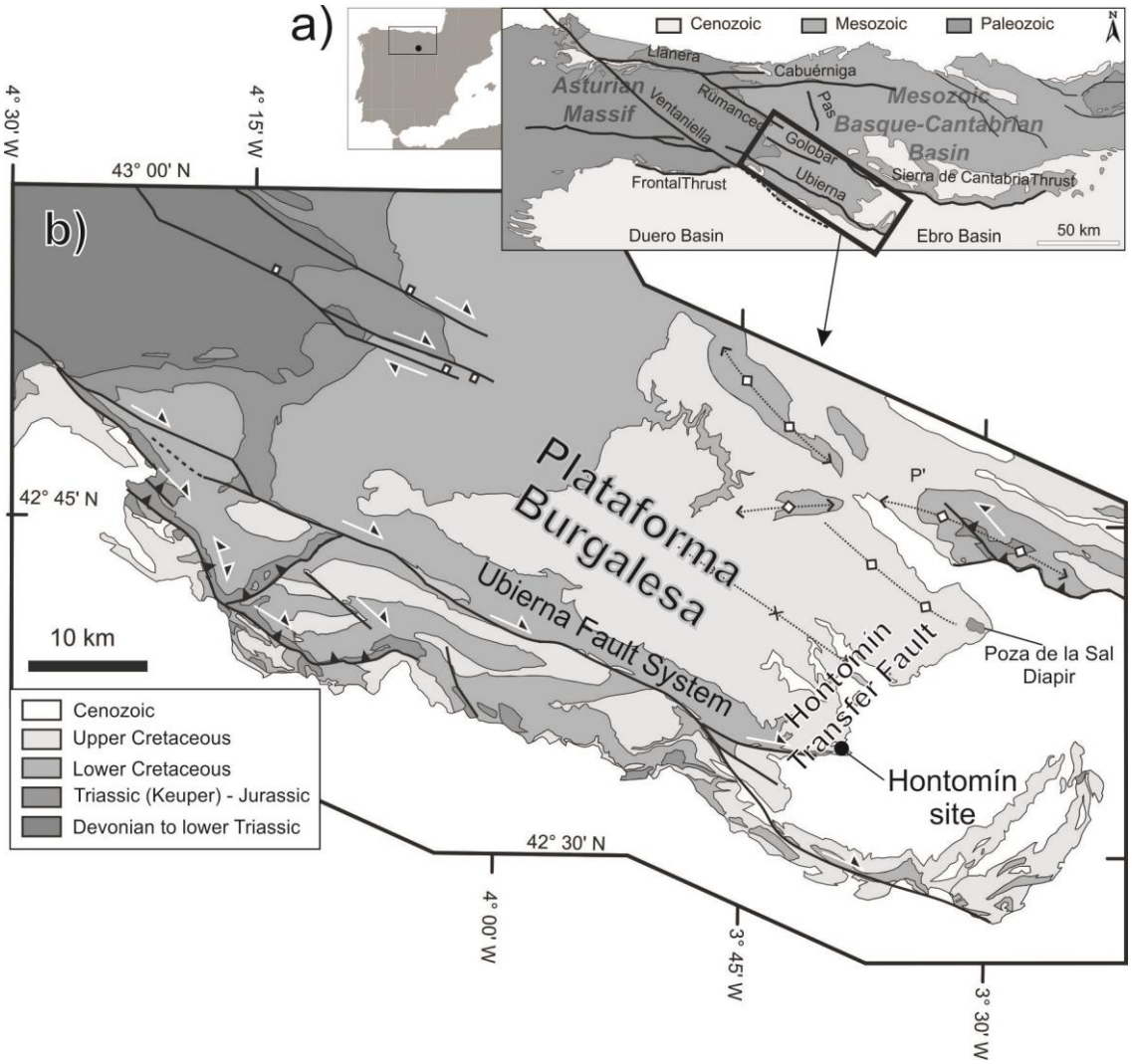
a)
Cenozoic
Mesozoic
Paleozoic
Llanera
Cabuérniga
Asturian Massif
Ventaniella
Rúmaceo
Pas
Mesozoic Basque-Cantabrian Basin
Golobar
Ubierna
Sierra de Cantabria Thrust
Frontal Thrust
Duero Basin
Ebro Basin
50 km
b)
4° 30' W
4° 15' W
43° 00' N
42° 45' N
42° 30' N
4° 00' W
3° 45' W
3° 30' W
Plataforma Burgalesa
Ubierna Fault System
Hontomín Transfer Fault
Poza de la Sal Diapir
Hontomín site
P'
10 km
Cenozoic
Upper Cretaceous
Lower Cretaceous
Triassic (Keuper) - Jurassic
Devonian to lower Triassic

81

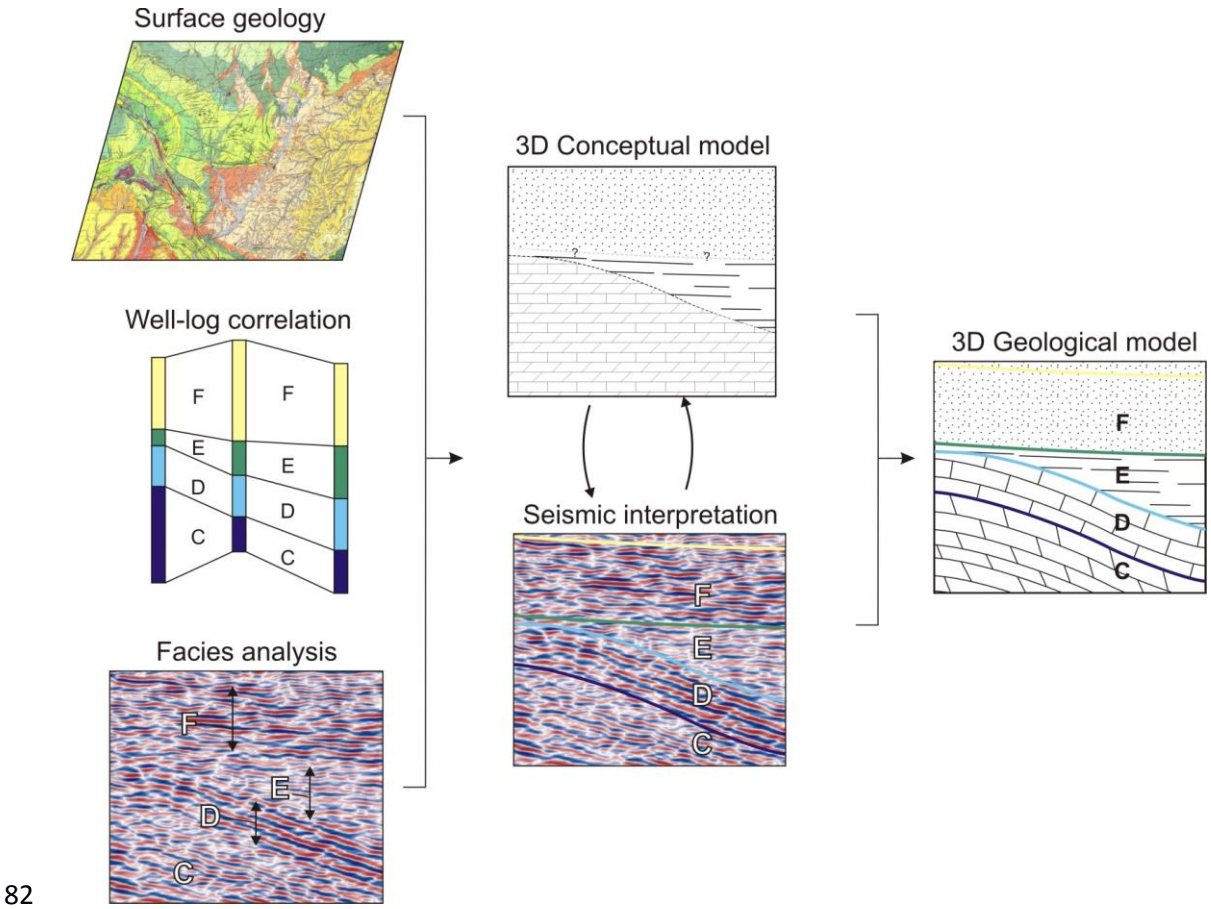
Surface geology
Well-log correlation
F
E
D
C
F
E
D
C
Facies analysis
F
E
D
C
3D Conceptual model
?
?
Seismic interpretation
F
E
D
C
3D Geological model
F
E
D
C

82
83

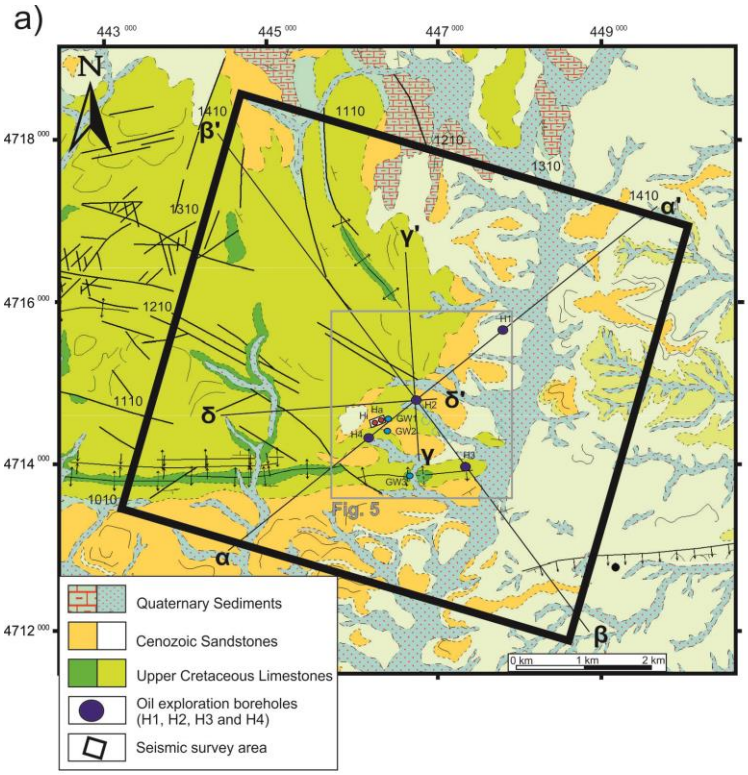
a)
443 000
445 000
447 000
449 000
4718 000
4716 000
4714 000
4712 000
N
1410
β'
1110
1210
1310
1410
α'
γ'
1310
1210
1110
δ
δ'
γ
1010
α
β
H1
H2
H3
H4
Ha
GW1
GW2
GW3
Fig. 5
0 km
1 km
2 km
Quaternary Sediments
Cenozoic Sandstones
Upper Cretaceous Limestones
Oil exploration boreholes
(H1, H2, H3 and H4)
Seismic survey area

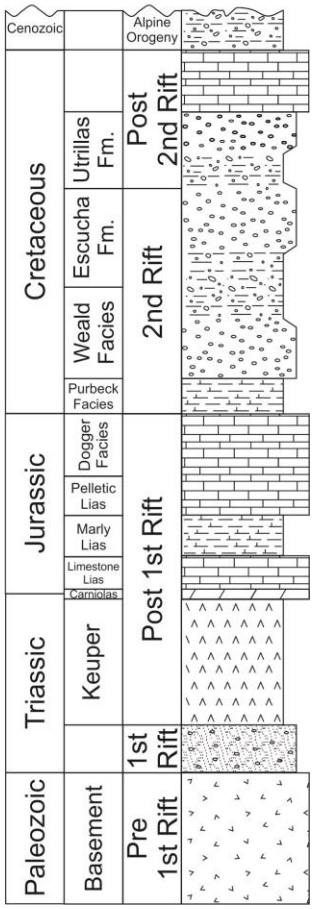
b)
Cenozoic
Alpine Orogeny
Cretaceous
Utrillas Fm.
Escucha Fm.
Weald Facies
Purbeck Facies
Post 2nd Rift
2nd Rift
Jurassic
Dogger Facies
Pelletic Lias
Marly Lias
Limestone Lias
Carniolas
Triassic
Keuper
Post 1st Rift
1st Rift
Paleozoic
Basement
Pre 1st Rift

84

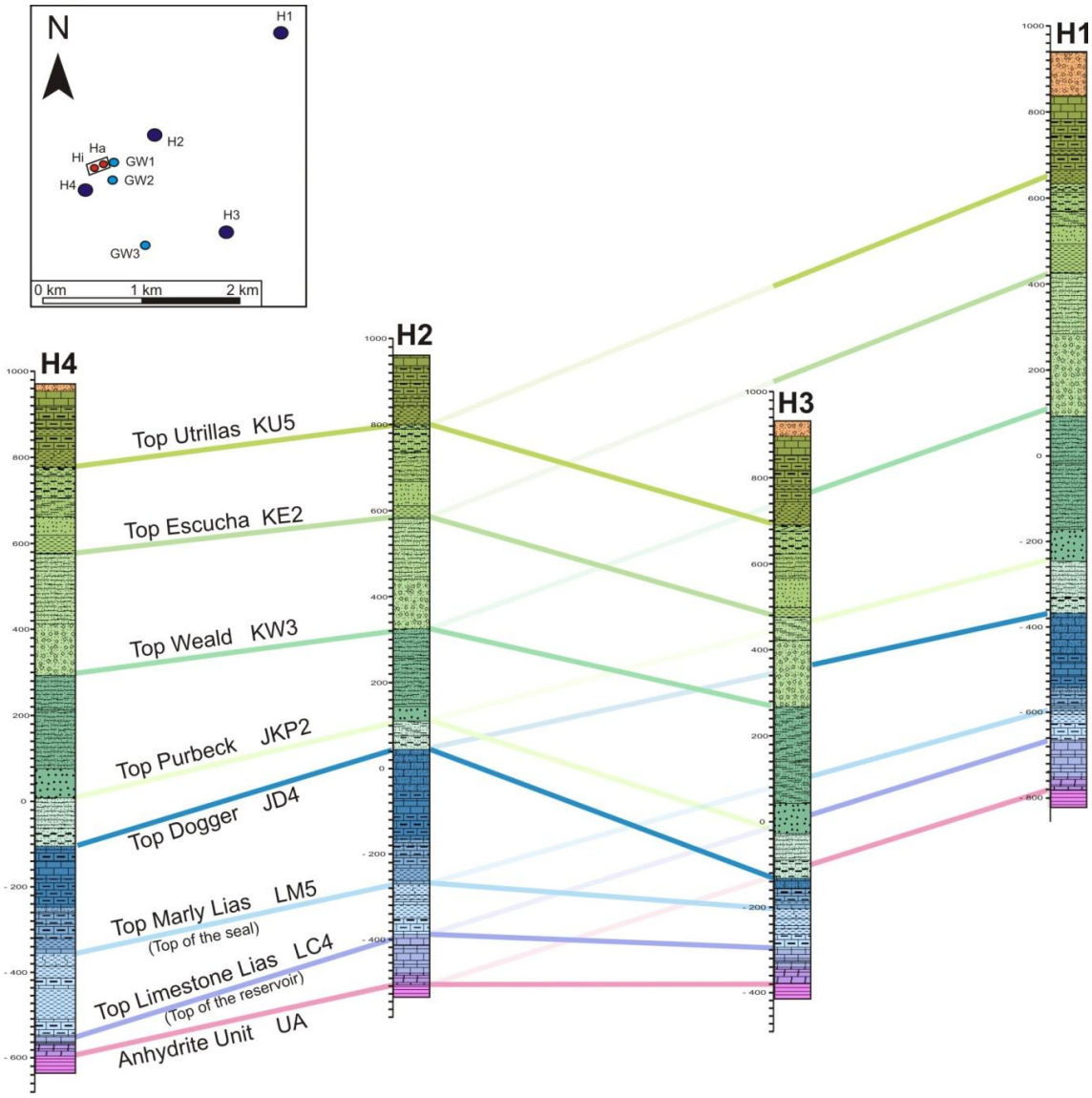
N
H1
H2
Ha
Hi
GW1
GW2
H4
H3
GW3
0 km
1 km
2 km
H4
H2
H3
H1
Top Utrillas KU5
Top Escucha KE2
Top Weald KW3
Top Purbeck JKP2
Top Dogger JD4
Top Marly Lias LM5
(Top of the seal)
Top Limestone Lias LC4
(Top of the reservoir)
Anhydrite Unit UA

85

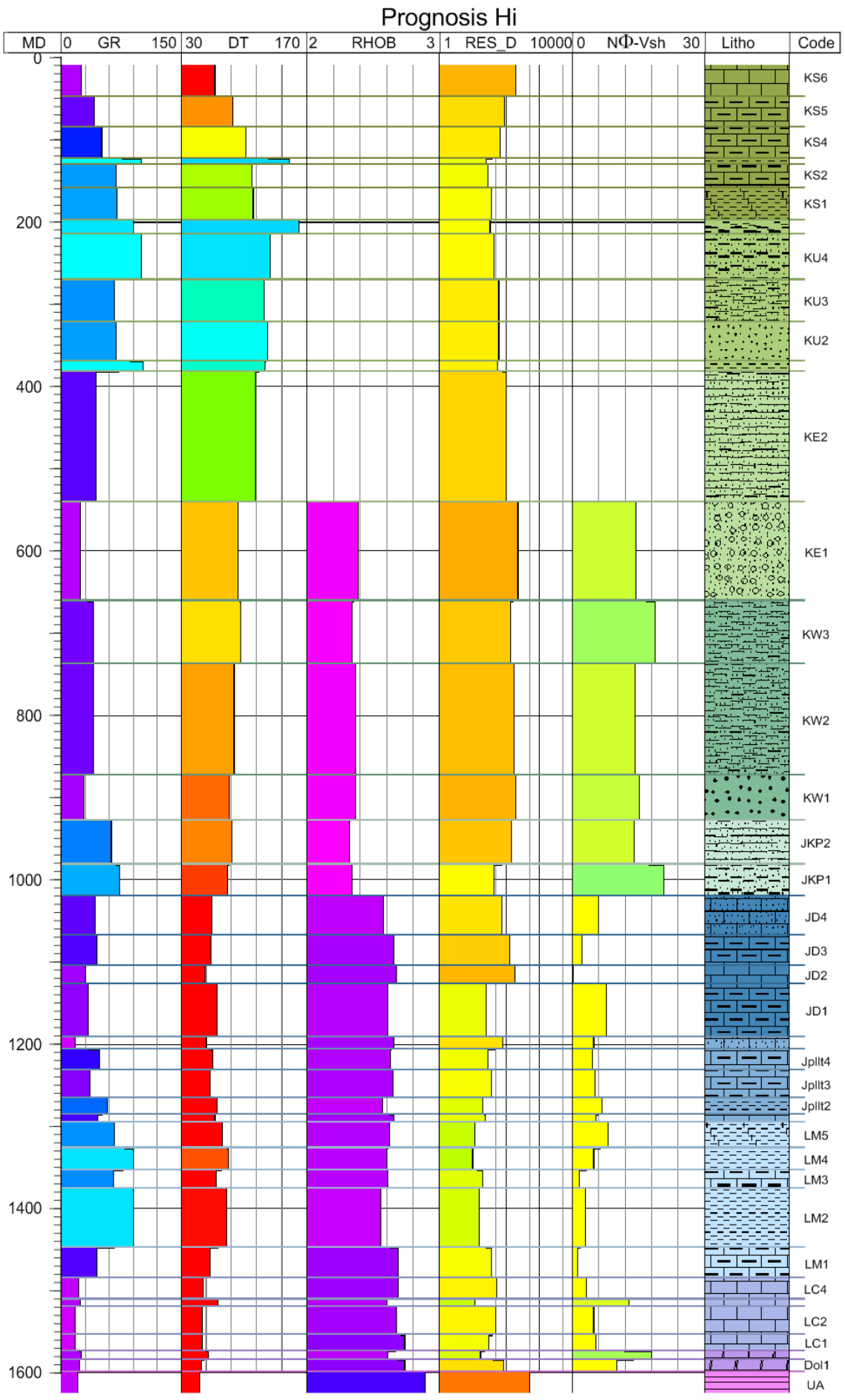
Prognosis Hi
MD
0 GR 150
30 DT 170
2 RHOB 3
1 RES_D 10000
0 NΦ-Vsh 30
Litho
Code
0
200
400
600
800
1000
1200
1400
1600
KS6
KS5
KS4
KS2
KS1
KU4
KU3
KU2
KE2
KE1
KW3
KW2
KW1
JKP2
JKP1
JD4
JD3
JD2
JD1
Jpllt4
Jpllt3
Jpllt2
LM5
LM4
LM3
LM2
LM1
LC4
LC2
LC1
Dol1
UA

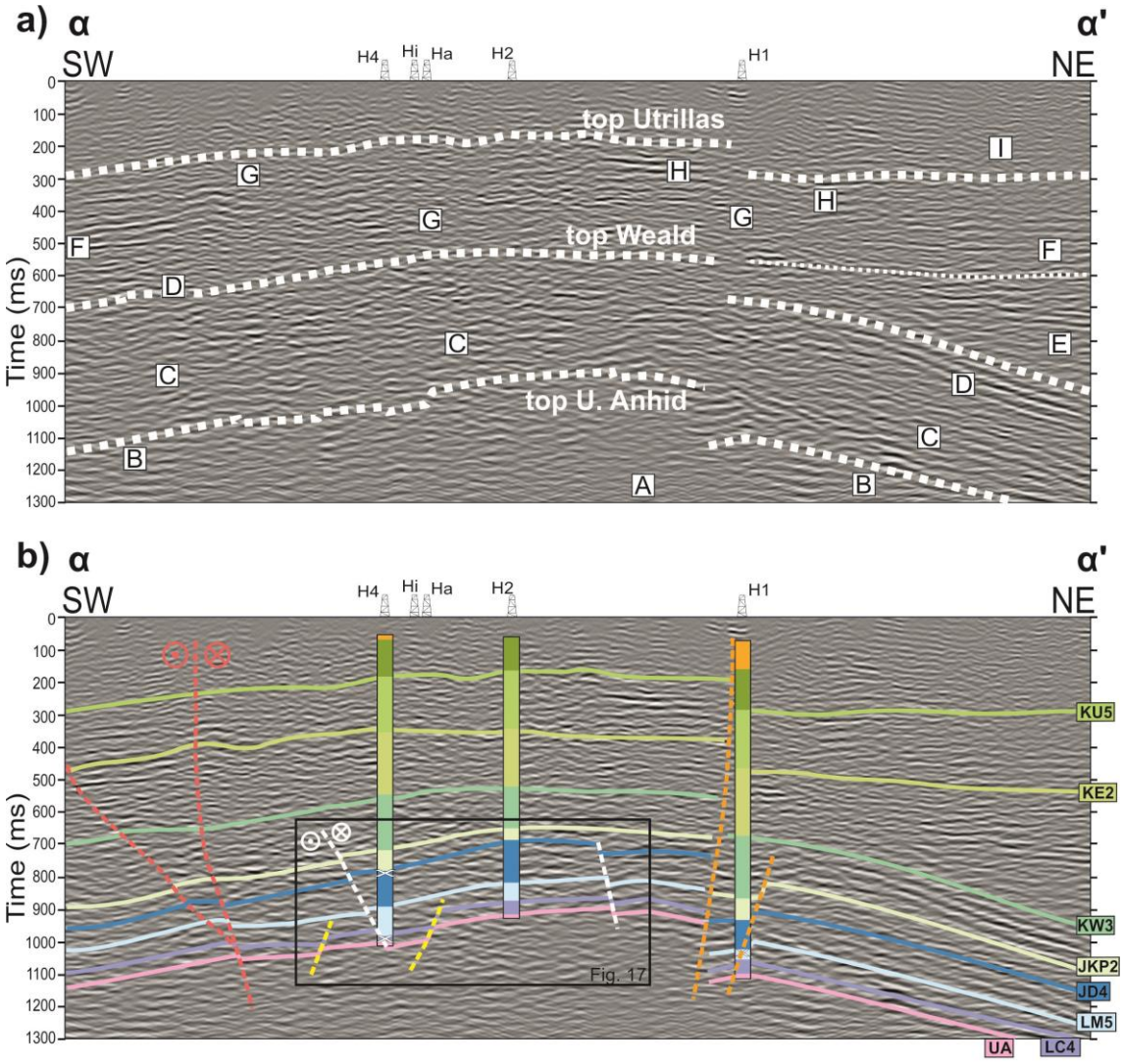
a) α
α'
SW
NE
H4
Hi
Ha
H2
H1
top Utrillas
top Weald
top U. Anhid
Time (ms)
b) α
α'
SW
NE
KU5
KE2
KW3
JKP2
JD4
LM5
UA
LC4
Fig. 17
Cenozoic
Upper Cretaceous
KU5: Top Utrillas
KE2: Top Escucha
KW3: Top Weald
JKP2: Top Purbeck
JD4: Top Dogger
LM5: Top Marly Lias (Seal)
LC4: Top Limestone Lias (Reservoir)
UA: Top Anhydrite Unit

87

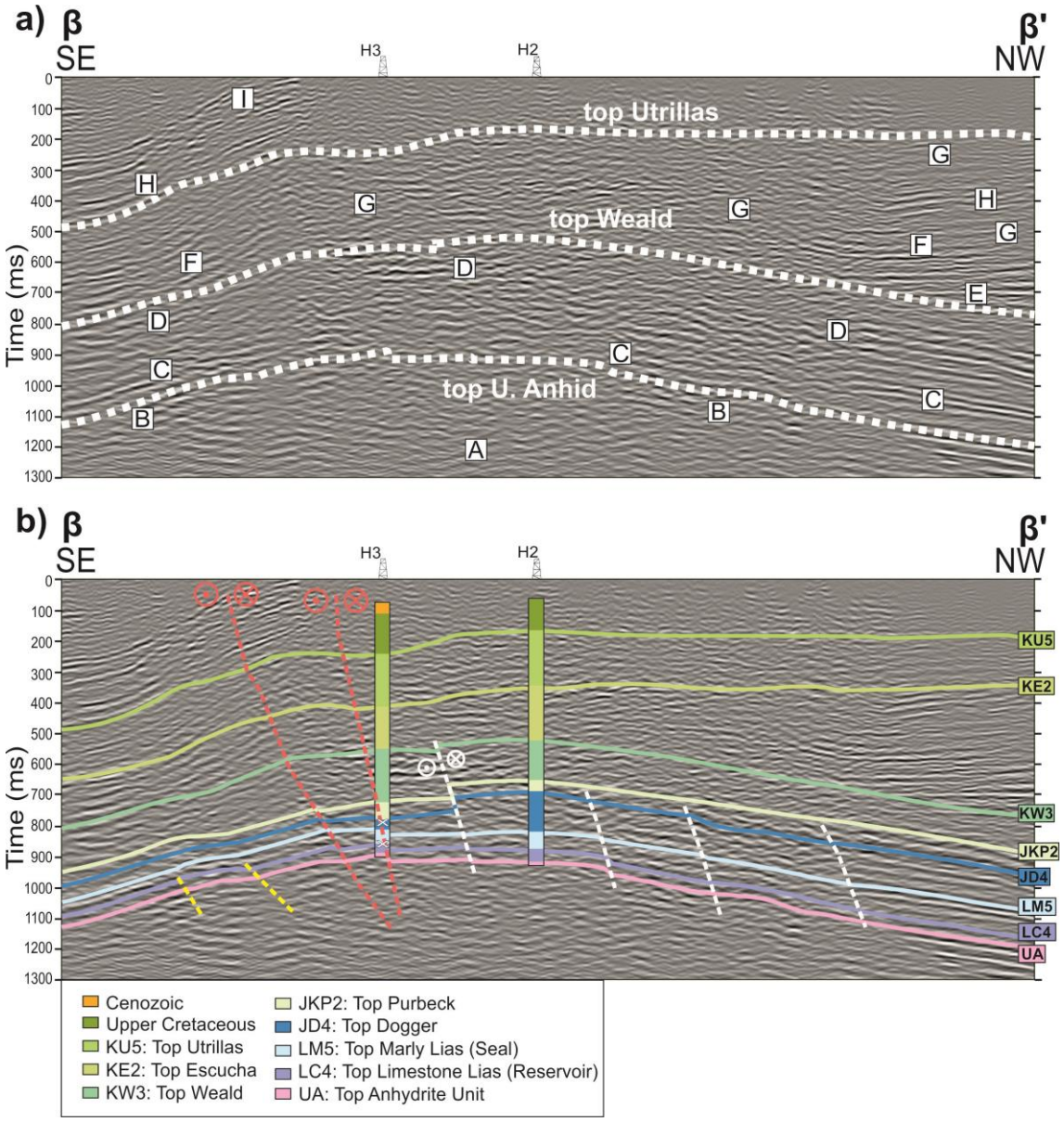
a) β
SE
H3
H2
β'
NW
Time (ms)
top Utrillas
top Weald
top U. Anhid
I
H
G
F
D
C
B
A
E
b) β
SE
H3
H2
β'
NW
Time (ms)
KU5
KE2
KW3
JKP2
JD4
LM5
LC4
UA
Cenozoic
Upper Cretaceous
KU5: Top Utrillas
KE2: Top Escucha
KW3: Top Weald
JKP2: Top Purbeck
JD4: Top Dogger
LM5: Top Marly Lias (Seal)
LC4: Top Limestone Lias (Reservoir)
UA: Top Anhydrite Unit

88

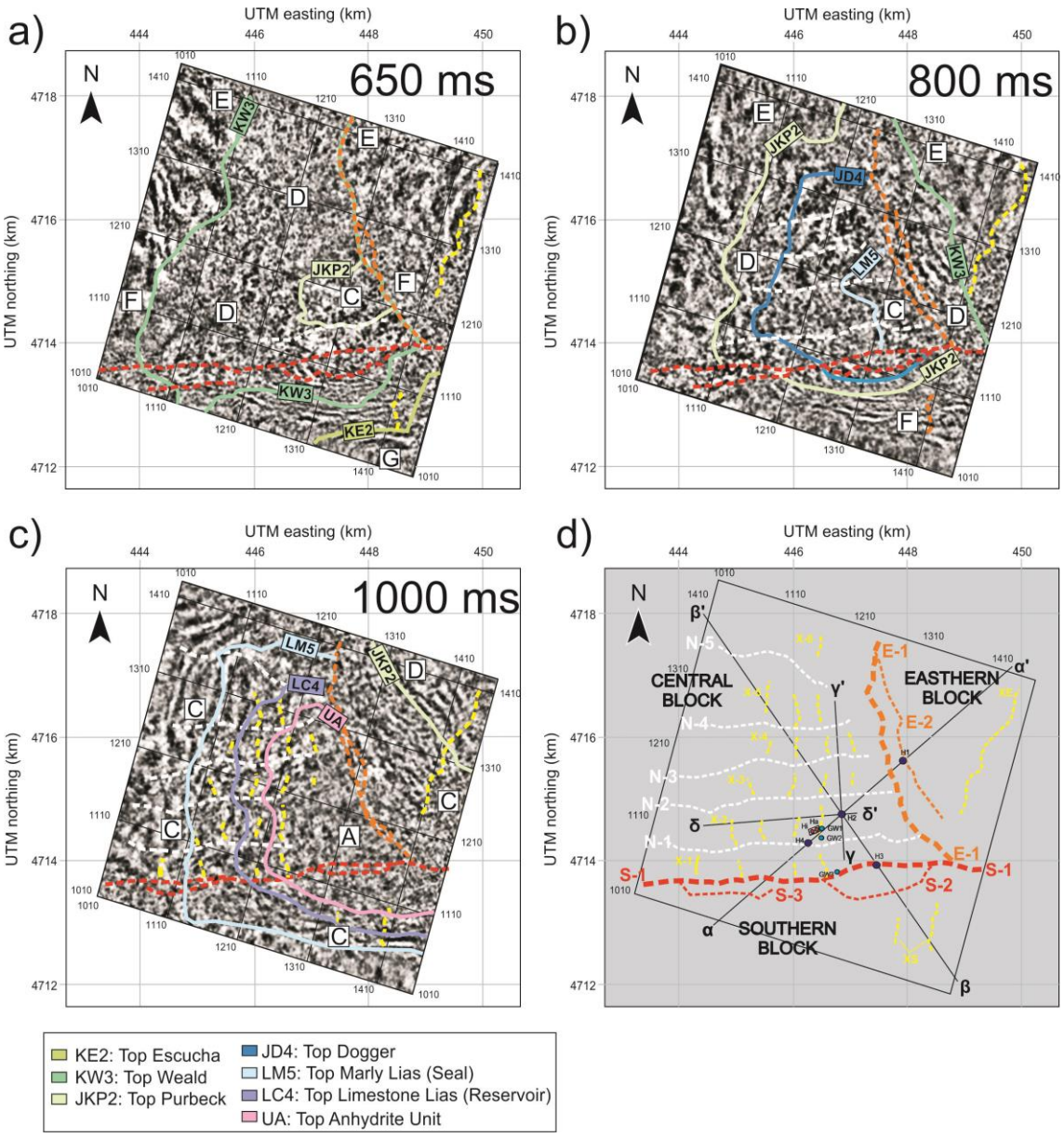
a)
UTM easting (km)
UTM northing (km)
650 ms
N
KW3
JKP2
KE2
b)
800 ms
JD4
LM5
c)
1000 ms
LC4
UA
d)
CENTRAL BLOCK
EASTHERN BLOCK
SOUTHERN BLOCK
E-1
E-2
S-1
S-2
S-3
N-5
N-4
N-3
N-2
N-1
KE2: Top Escucha
KW3: Top Weald
JKP2: Top Purbeck
JD4: Top Dogger
LM5: Top Marly Lias (Seal)
LC4: Top Limestone Lias (Reservoir)
UA: Top Anhydrite Unit

89

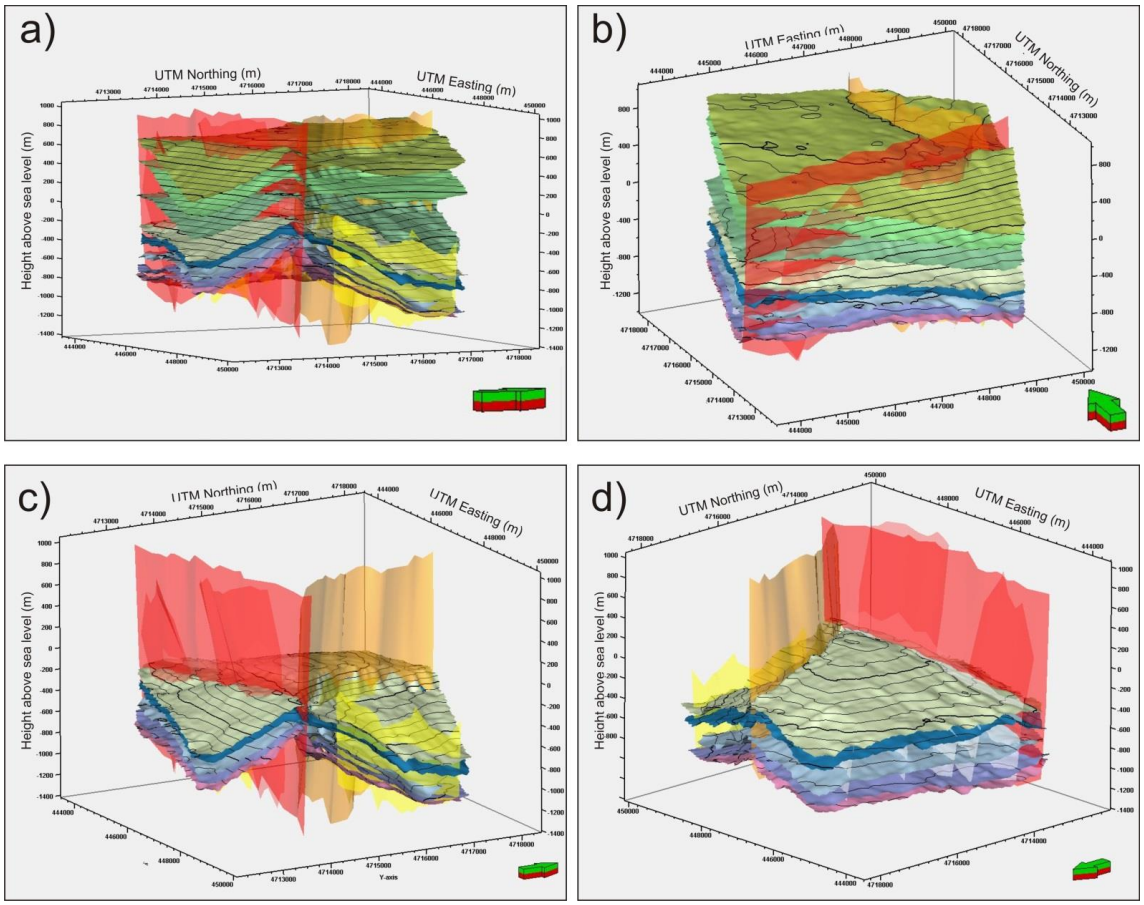
a)
UTM Northing (m)
UTM Easting (m)
Height above sea level (m)
b)
UTM Easting (m)
UTM Northing (m)
Height above sea level (m)
c)
UTM Northing (m)
UTM Easting (m)
Height above sea level (m)
d)
UTM Northing (m)
UTM Easting (m)
Height above sea level (m)

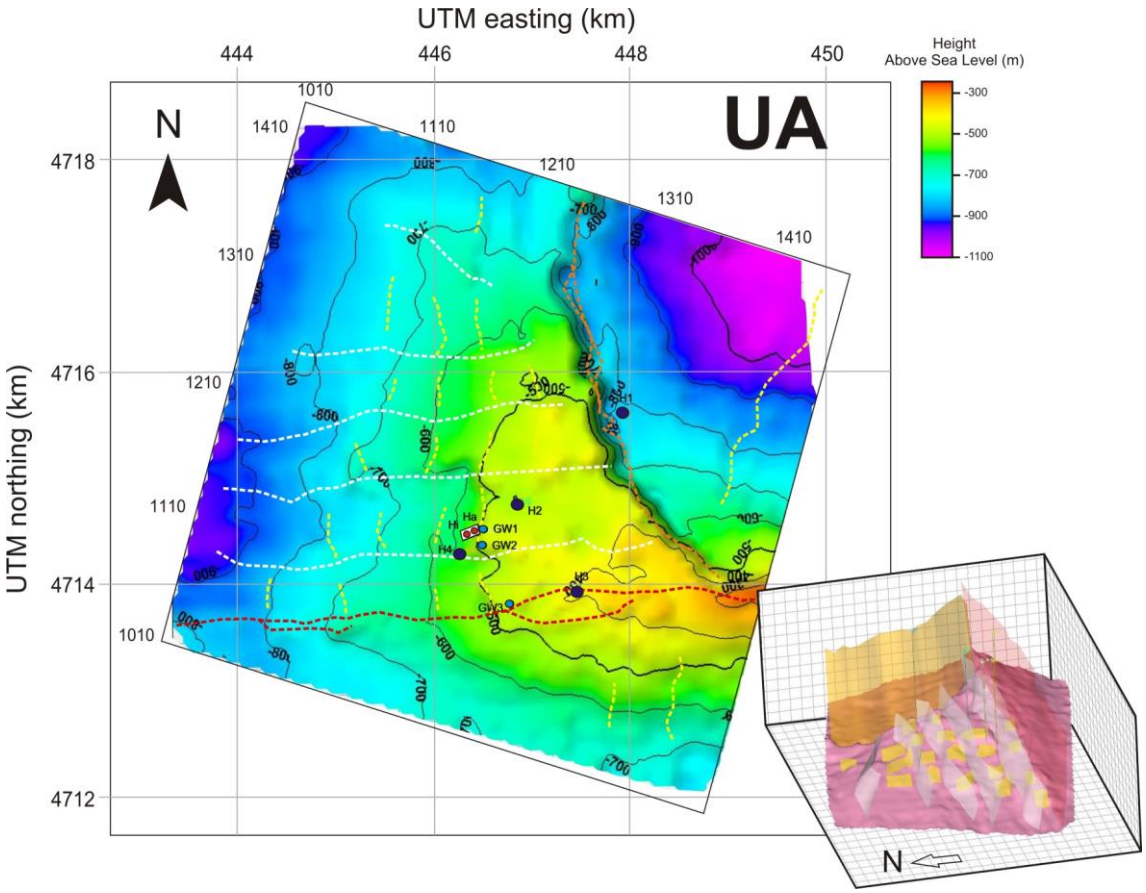
UTM easting (km)
444
446
448
450
UTM northing (km)
4718
4716
4714
4712
N
UA
Height
Above Sea Level (m)
-300
-500
-700
-900
-1100
1010
1410
1110
1210
1310
1410
1310
1210
1110
1010
H1
H2
Ha
Hi
GW1
GW2
H4
GW3
H5
N

92
93

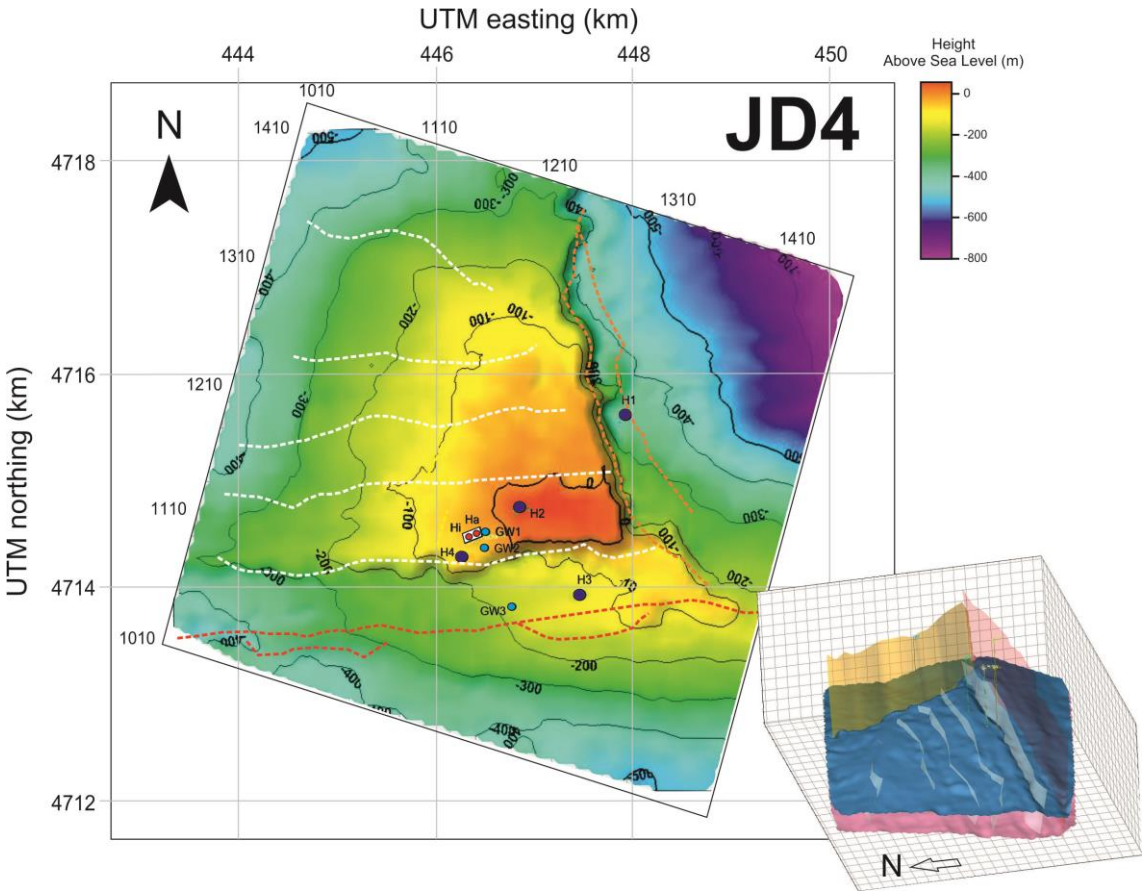
UTM easting (km)
444
446
448
450
UTM northing (km)
4718
4716
4714
4712
N
JD4
Height
Above Sea Level (m)
0
-200
-400
-600
-800
1010
1110
1210
1310
1410
H1
H2
H3
H4
Ha
Hi
GW1
GW2
GW3
N

94
95

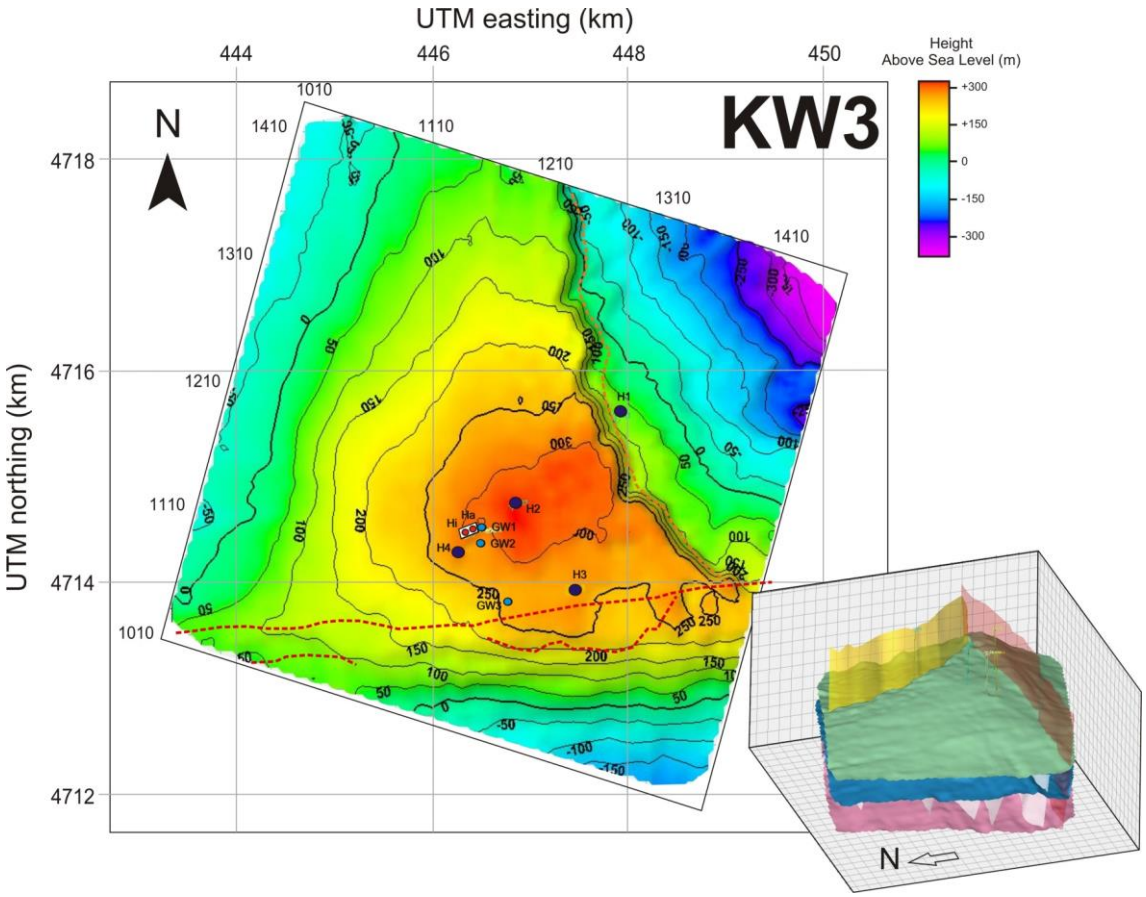
UTM easting (km)
444
446
448
450
UTM northing (km)
4718
4716
4714
4712
N
KW3
Height
Above Sea Level (m)
+300
+150
0
-150
-300
H1
H2
H3
H4
Ha
Hi
GW1
GW2
GW3
N

96
97

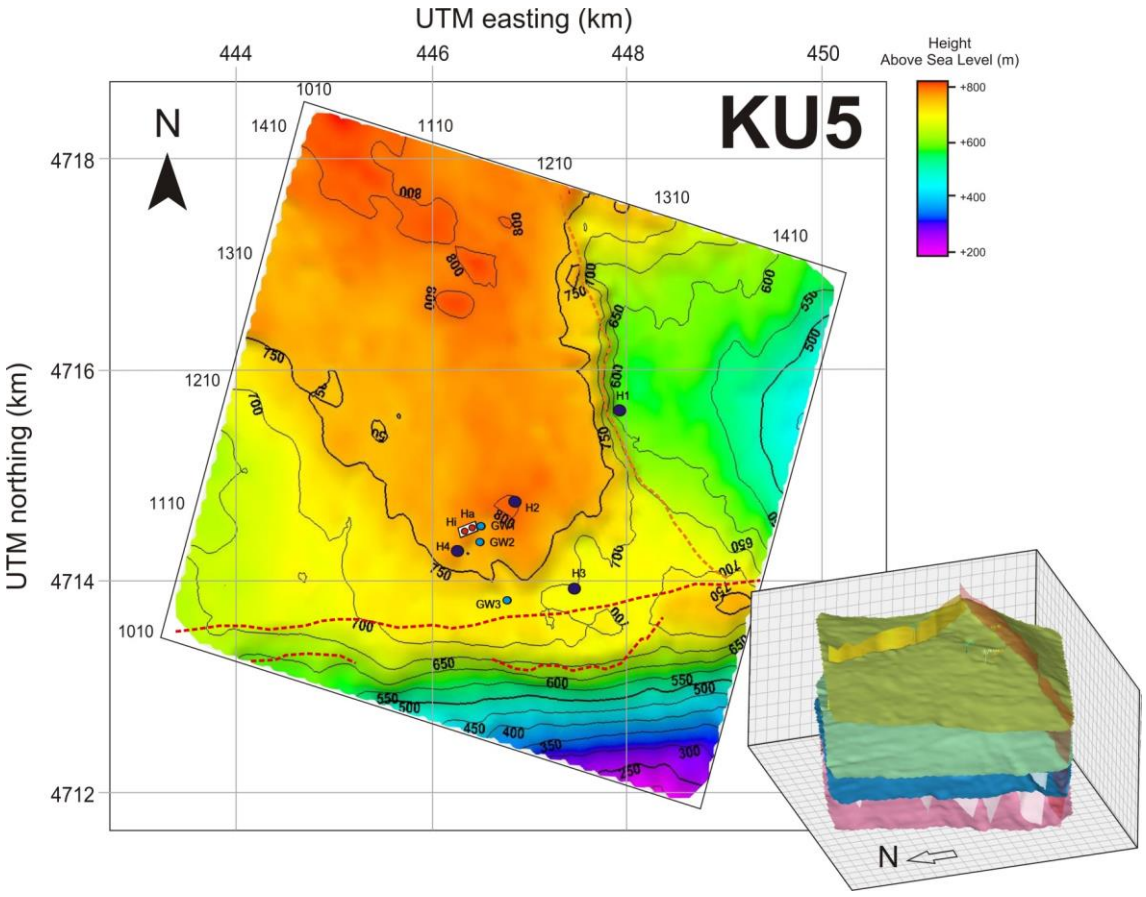
UTM easting (km)
444
446
448
450
UTM northing (km)
4718
4716
4714
4712
KU5
N
Height
Above Sea Level (m)
+800
+600
+400
+200
H1
H2
H3
H4
Ha
GW1
GW2
GW3
N

98

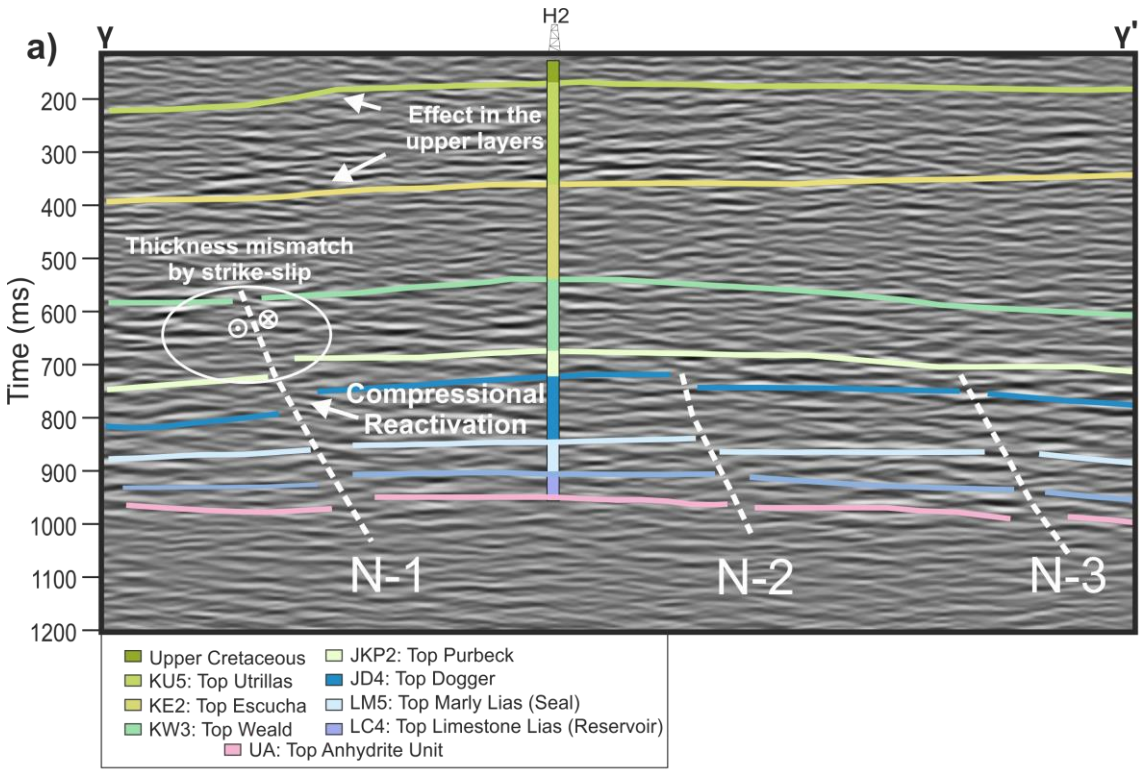
a)
Y
H2
Y'
Effect in the upper layers
Thickness mismatch by strike-slip
Compressional Reactivation
N-1
N-2
N-3
Time (ms)
200
300
400
500
600
700
800
900
1000
1100
1200
Upper Cretaceous
KU5: Top Utrillas
KE2: Top Escucha
KW3: Top Weald
UA: Top Anhydrite Unit
JKP2: Top Purbeck
JD4: Top Dogger
LM5: Top Marly Lias (Seal)
LC4: Top Limestone Lias (Reservoir)

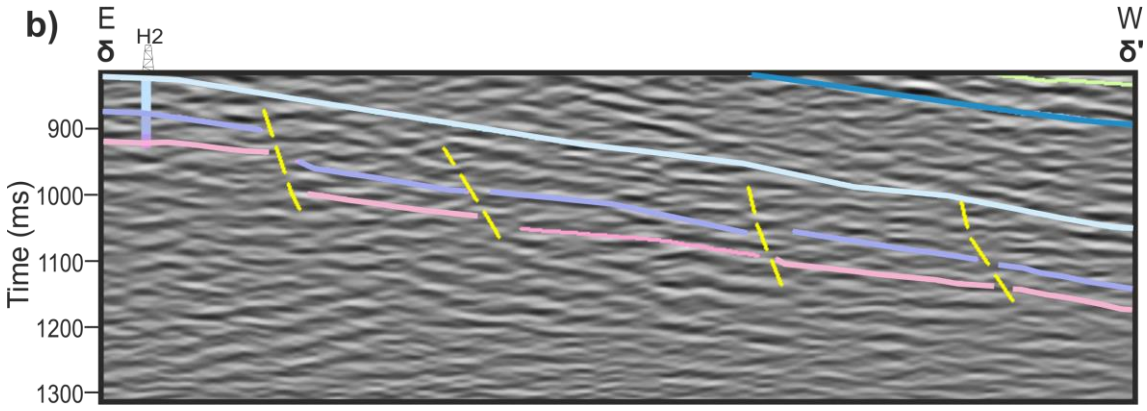
b)
E
δ
H2
W
δ'
Time (ms)
900
1000
1100
1200
1300

99

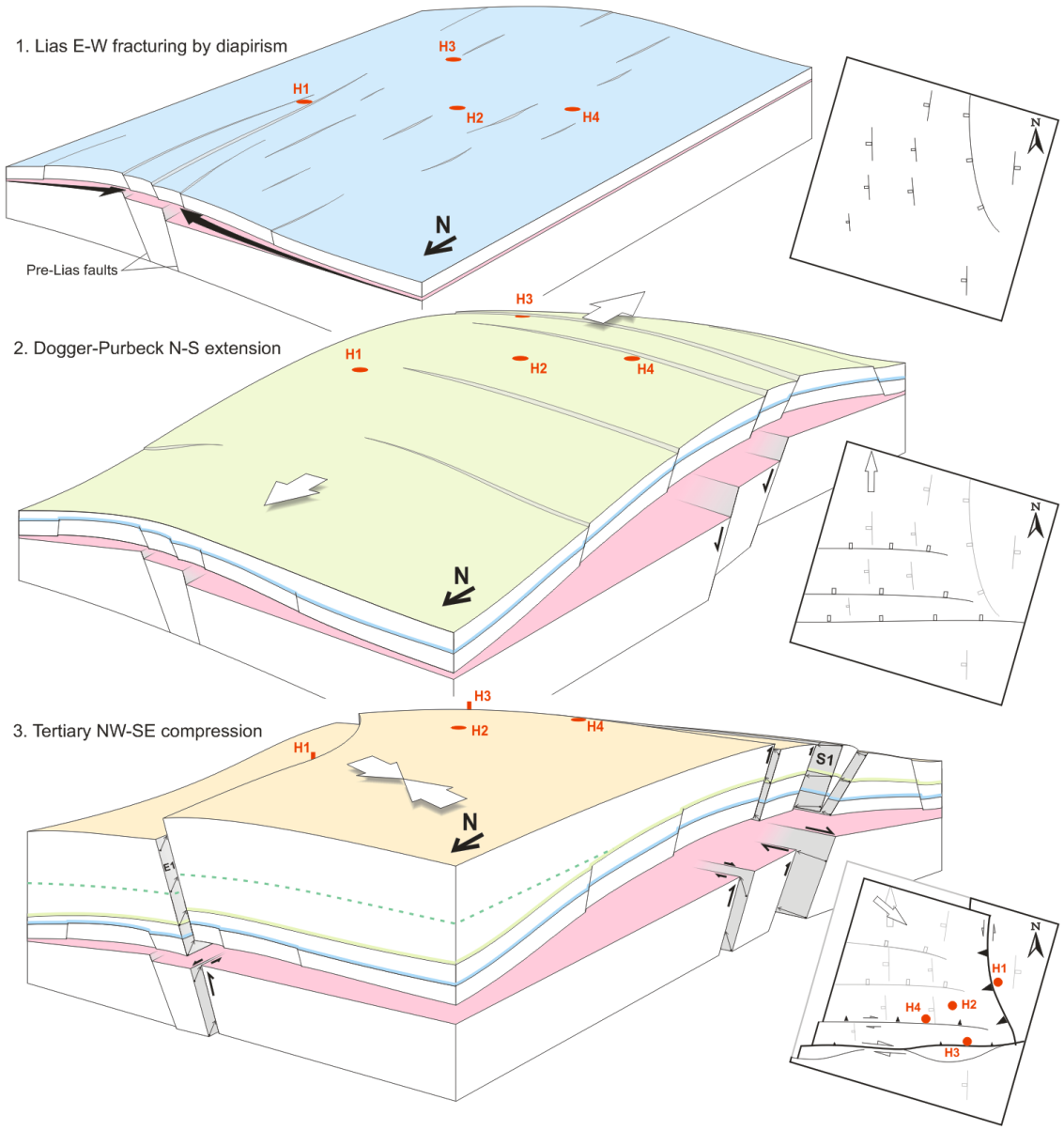
1. Lias E-W fracturing by diapirism
H3
H1
H2
H4
N
Pre-Lias faults
N
2. Dogger-Purbeck N-S extension
H3
H1
H2
H4
N
N
3. Tertiary NW-SE compression
H3
H2
H4
H1
S1
N
N
H1
H4
H2
H3

100
101

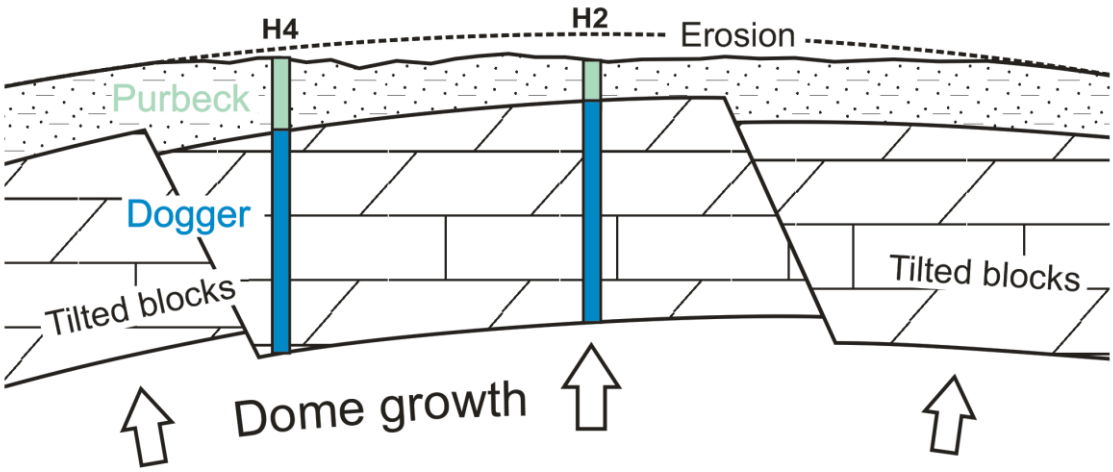
H4
H2
Erosion
Purbeck
Dogger
Tilted blocks
Tilted blocks
Dome growth

102
103

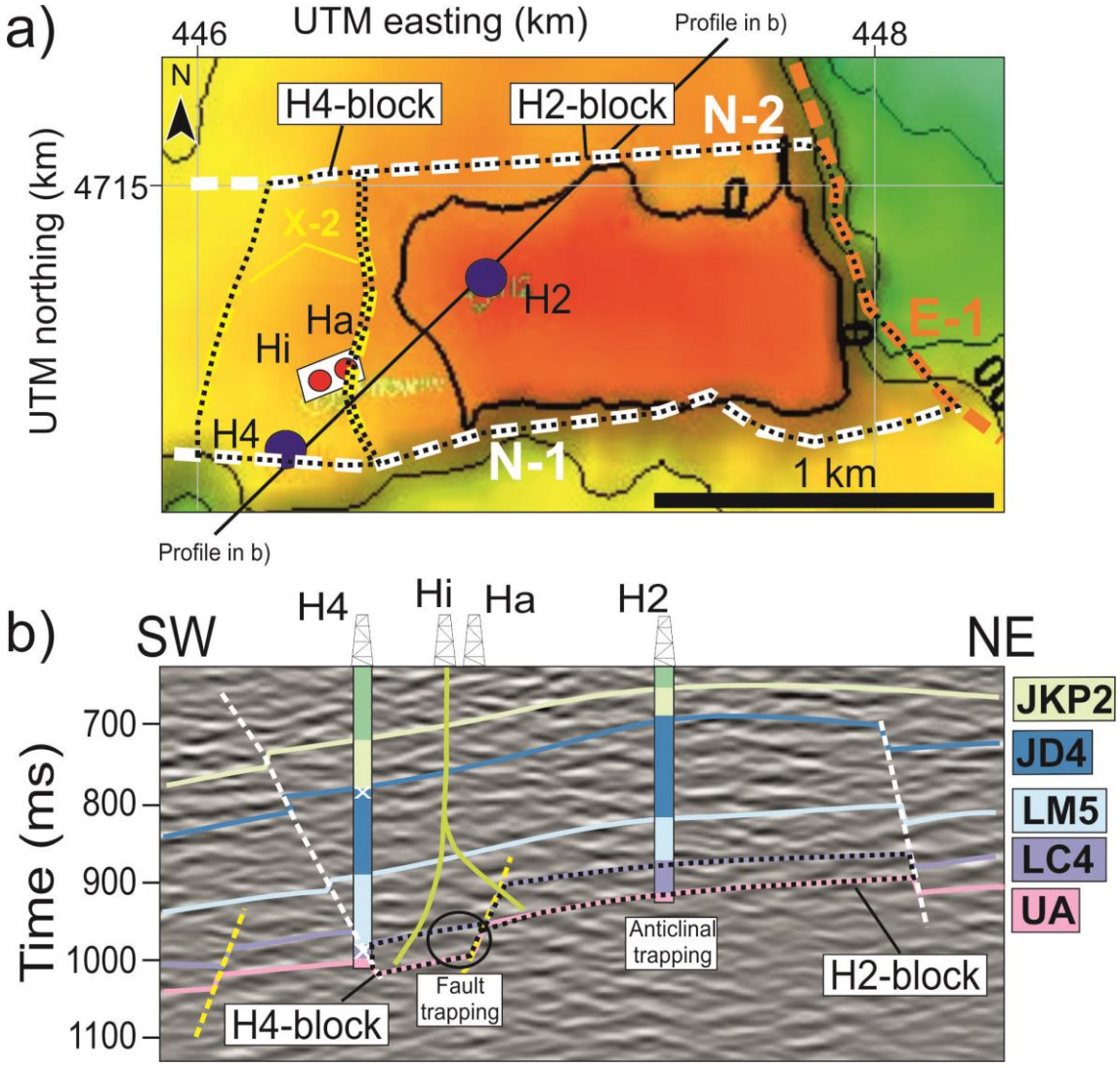
a)
446
UTM easting (km)
Profile in b)
448
N
H4-block
H2-block
N-2
UTM northing (km)
4715
X-2
H2
Ha
Hi
E-1
H4
N-1
1 km
Profile in b)
b)
SW
H4
Hi
Ha
H2
NE
JKP2
JD4
LM5
LC4
UA
Time (ms)
700
800
900
1000
1100
Anticlinal trapping
Fault trapping
H4-block
H2-block

104

Supplementary material captions

SM1: 3D interactive visualization of the resulting geological model. It includes the 8 geological layers (Anhydrite Unit – UA; Top Limestone Lias – LC4; Top Marly Lias – LM5; Top Dogger – JD4; Top Purbeck – JKP2; Top Weald – KW3; Top Escucha – KE2; and Top Utrillas – KU5) and the 4 fault sets (set X, set N, set S and set E) interpreted.